EFFECTS OF EQUAL CHANNEL ANGULAR EXTRUSION ON THE MICROSTRUCTURE AND MECHANICAL PROPERTIES OF CoCrFeMnNi

A Thesis

by

HAVVA CANSU YILMAZ

Submitted to the Office of Graduate and Professional Studies of
Texas A&M University
in partial fulfillment of the requirements for the degree of

MASTER OF SCIENCE

Chair of Committee,	Ibrahim Karaman
Committee Members,	Tahir Cagin
	Homero Castaneda-Lopez
Head of Department,	Ibrahim Karaman

December 2017

Major Subject: Materials Science and Engineering

ABSTRACT

The present work aims at revealing the effect of grain size on the post processing mechanical behavior of the equiatomic CoCrFeMnNi high entropy alloy (HEA) upon severe plastic deformation (SPD). SPD has been applied using the equal channel angular extrusion (ECAE) process where the billets are extruded through a 90° corner die achieving near simple shear deformation. The microstructure and mechanical properties of successfully extruded billets were reported using Scanning Electron Microscopy (SEM), Transmission Electron Microscopy (TEM), Energy Dispersive Spectroscopy (EDS), tension experiments and microhardness measurements. The effects of extrusion conditions, such as temperature, processing route and extrusion rate on the microstructure and mechanical properties, are investigated for the extrusion and flow plane of each billet. The ECAE deformation of CoCrFeMnNi at high homologous temperatures results in deformation twinning. Refined mean grain size leads to significant increase in tensile flow stresses at room temperature. Further work is needed to find processing schedules at low temperatures to refine the grain size further to determine the lower limit of grain size one can achieve in bulk HEAs.

To My Family

ACKOWLEDGEMENTS

First of all, I would like to thank Dr. Ibrahim Karaman for not only being my advisor but also for his great guidance during my education at Texas A&M University. He has helped me enormously in all aspects of this project and improving my technical skills in this field. Without his mentorship, this project would not have been completed.

I would like to thank my committee members, Dr. Cagin and Dr. Castaneda for sharing their valuable comments and suggestions about my thesis. I would also like to thank for their constructive comments on my thesis.

I am grateful to Dr. Canadinc for his guidance in my research and sharing his deep knowledge on TEM results. Dr. Liu is thanked for his assistance in TEM imaging. I am also thankful to Mr. Robert Barber and Mr. Michael Elverud for helping me with the preparation of the samples before and after the ECAE process.

Special thanks to my friends, Sezer Picak, Tejas Umale, Wahaz Nasim, Abhinav Srivastava and Daniel Salas Mula for their precious help on the experiments and valuable discussions. Their support eased the difficulties during my research. They were always helpful in introducing their own cultures and broadening my horizon. Melek Bulanik and Kubra Sila Kilic are more like sisters to me. We have been far apart for years, even living in different continents; however, you have always been beside me. Thank you for making me feel at home with your never-ending support and belief in my endeavors.

I would like to thank Ata Firat Pir for being there whenever I need him and encouraging me to become the person I want to be. Thank you for making me more than I am.

My deepest gratitude to my family, Ayten Yilmaz, Efendi Yilmaz, Serkan Yilmaz, Efsun Yilmaz Ugur, Hakan Ugur and Duru Neva Ugur for their never-ending support and trust which makes life easier for me. I have always felt very lucky for having them.

CONTRIBUTORS AND FUNDING SOURCES

Contributors

This work was supported by a thesis committee consisting of Dr. Ibrahim Karaman, Dr. Tahir Cagin and Dr. Homero Castaneda of the department of Materials Science and Engineering.

TEM images analyzed for the entire work was provided by Dr. Jun Liu.

All other work conducted for the thesis was completed by the student independently.

Funding Sources

Graduate study was supported by a fellowship from Turkish Petroleum International Company.

TABLE OF CONTENTS

Page

Page

LIST OF FIGURES

Page

Page

Page

Page

LIST OF TABLES

Page

CHAPTER I

INTRODUCTION

1.1 History and Background on High-Entropy Alloys

In history, most scientists in materials science tried to design and produce enormous alloys depending on one principal element and one or more minor element/elements, which are called traditional alloys. In the twenty-first century, two scientists named Brian Cantor and Jien-Wei Yeh independently made a groundbreaking discovery apart from traditional alloys [1-6]. It was the first time some of the multi-phase alloys were coined as high-entropy alloys (HEAs).

Brian Cantor and his student Alain Vincent made several equiatomic alloys by mixing at least 5 and even up to 20 components. In [1], it was observed that only equiatomic CoCrFeMnNi formed a single-phase dendritic FCC structure, and the lattice parameters of CoCrFeMnNi were calculated with X-ray diffraction experiment. In that study, there were many significant conclusions. The first conclusion was that adding some other components, such as Cu, V, Mo and Ge, to CoCrFeMnNi indicated the same majority FCC phase, yet adding more electronegative components made the alloy less stable than others. Cantor also proved this claim with Gibbs phase rules [1]. Another important conclusion was that alloys with 20 and 16 components were multi-phase as opposed to other alloys. Nevertheless, the alloys containing more components that are especially rich in Cr, Mn, Fe, Co, Ni mainly showed FCC structure [1, 7].

Another scientist, Jien-Wei Yeh, who studied multi-component alloy systems, showed that high mixing entropy is significant for single-phase alloys. He stated that achieving enough high mixing entropy in experiments could reduce the number of phases in an alloy which is essential for outstanding properties of material. By using the arc melting technique, 40 equiatomic alloys with five to nine components were fabricated. In his first study, Yeh focused on the hardness of the HEAs and concluded that except for the nine-element HEAs, if the number of the components increases, the hardness of the alloy also increases. Moreover, the addition of the element B also increases the hardness of the alloy. In addition to hardness experiments, his research team also conducted studies of wear behavior, annealing behavior, deformation behavior, and thin film deposition and coating of HAEs studies. All fabricated HEAs showed excellent corrosion resistance despite strong acidic solutions such as HCl, HF, H_2SO_4 and HNO_3. With these experiments, he introduced HEAs with their unique properties such as high-entropy effect, lattice distortion effect, slow diffusion effect and cocktail effect.

Following the history of HEAs, it is important to mention their concept and definition as well. Yeh introduced HEAs [6] as the alloys that consist of at least five principal components in equimolar ratios or near-equimolar ratios, where the atomic percentage of each element ranges between 5% and 35%. As opposed to traditional alloys, HEAs tend to form simple solid-solution phases. This tendency results in high mixing entropy and the term 'high-entropy' comes from this inherent behavior [2-8]. From thermodynamics, any alloy system achieves equilibrium state when differences in Gibbs free energy, ΔG_{mix}, at any two different states reach a minimum value. Equation 1.1 gives a formula for ΔG_{mix},

$$\Delta G_{mix} = \Delta H_{mix} - T\Delta S_{mix} \quad (1.1)$$

where ΔH_{mix}, ΔS_{mix} and T are the difference in enthalpy, the difference in entropy, and temperature, respectively [9-11]. Boltzmann's equation can be used to find a relationship between entropy and system parameters,

$$\Delta S_{conf} = k \ln w \quad (1.2)$$

where ΔS_{conf} is the difference in configurational entropy per mole of a system, k is the Boltzmann's constant, and w is the number of microstates that are consistent with the given macrostate [11]. Even though the mixing entropy consists of four contributors, configurational entropy dominates the other three contributors. Therefore, mixing entropy is often replaced by configurational entropy to be in tune with the literature of HEAs [6, 12, 13].

Equation 1.2 can be defined in terms of the number of different elements n, and mole fractions of i-th element X_i as follows:

$$\Delta S_{conf} = -R \sum_{i=1}^{n} X_i \ln X_i$$

where $R = 8.31 \left[\frac{Jolue}{Mol.K}\right]$ is the gas constant. In [6], Yeh suggested a new approach to the mixing entropy of multi-phase alloys in equimolar or near-equimolar conditions, calculated below.

$$X_1 = X_2 = \cdots = X_n$$

$$X_1 = \frac{1}{n}$$

$$\Delta S_{conf} = -R \sum_{i=1}^{n} \frac{1}{n} lnX_i = -R\left(\frac{1}{n}\ln\frac{1}{n} + \frac{1}{n}\ln\frac{1}{n} + \cdots + \frac{1}{n}\ln\frac{1}{n}\right)$$

$$\Delta S_{conf} = -R\ln\frac{1}{n} = R\ln n$$

Table 1.1 and Figure 1.1 show that for any alloy system, ΔS_{conf} increases when n increases, as expected [2, 6, 7].

Table 1.1 ΔS_{conf} of equimolar alloys with up to 8 elements.

n	1	2	3	4	5	6	7	8
ΔS_{conf}	0	0.69R	1.1R	1.39R	1.61R	1.79R	1.95R	2.08R
ΔS_{conf}	0	5.76	9.13	11.52	13.37	14.89	16.17	17.38

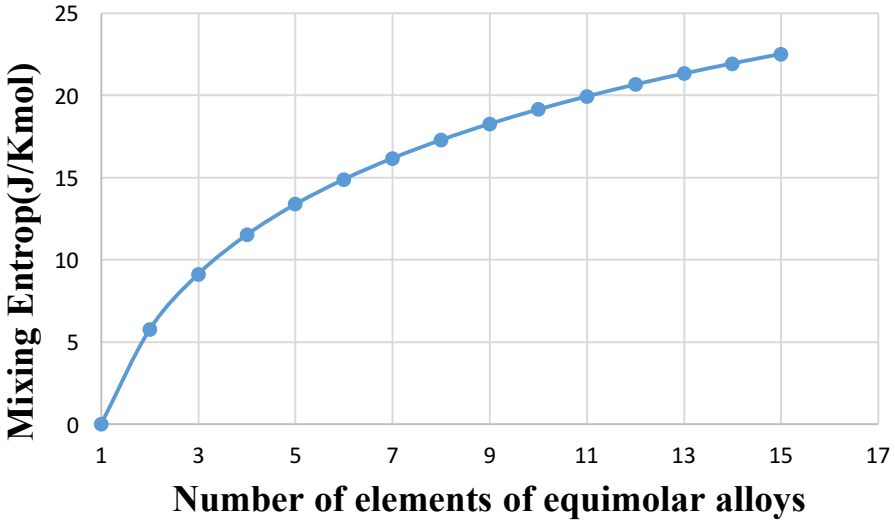

Figure 1.1 ΔS_{mix} as a function of n for equiatomic alloys.

By Richard's rule, during the melting process, ΔS_{mix} can be named as ΔS_{fusion} which is approximately the gas constant R for metals [11].

$$\Delta S_{fusion} = 2.2 \frac{cal.K}{mol} = 9.204 \frac{Joule.K}{mol} \approx R \tag{1.3}$$

During melting, the correlation between entropy change and enthalpy change can be defined as below.

$$\Delta G_{fusion} = \Delta H_{fusion} - T_m \Delta S_{fusion} \tag{1.4}$$

Here ΔG_{fusion}, ΔH_{fusion} and T_m are the difference in Gibbs free energy at a melting point, the difference in enthalpy at a melting point or latent heat, and the melting temperature of an alloy, respectively. Since ΔG_{fusion} is zero during a melting process, Equation 1.4 can be deduced to the following equation.

$$\Delta H_{fusion} = T_m \Delta S_{fusion} \tag{1.5}$$

Due to the difference in bond at liquid and solid state, ΔH_{fusion} is required to break nearly one-twelfth of the bonds in the closed packed structure per mole.

$$\Delta H_{fusion} \approx \frac{E_{bond}}{12} \tag{1.6}$$

If Equation 1.3 and Equation 1.6 are substituted in Equation 1.5, we can achieve Equation 1.7 [13]. The gas constant R is significant in order to achieve equilibrium state by reducing Gibbs free energy sharply. There is a strong direct relationship between bond strength and melting temperature of the material.

$$\frac{E_{bond}}{12} = T_m R \tag{1.7}$$

As mentioned before, Yeh defined HEAs for major elements. In addition to these major elements, if there is any minor element in the alloy, its atomic percentage should be less than 5% [3, 13]. The definition can be expressed as below.

$$n_{major} \geq 5$$

$$5\% \leq X_i \leq 35\%$$

$$n_{minor} \geq 0$$

$$X_j \leq 5\%$$

Here n_{major} and n_{minor} denote the number of major and minor elements, whose atomic percentages are X_i and X_j, respectively [3, 13].

HEAs can also be defined as the alloys that have configurational entropies greater than or equal to $1.5R$ at a random solution state [3, 13]. In Table 1.1, the mixing entropy value for five elements is equal to $1.61R$. Yeh explained the reason why the lower limit is $1.5R$ instead of $1.61R$ is because the latter is for equiatomic HEAs, whereas the values between $1.5R$ and $1.61R$ are for non-equiatomic alloys. Therefore, to cover all types of HEAs (equiatomic and non-equiatomic), the lower limit is taken to be $1.5R$. To illustrate that, for equimolar CrCuFeMnNi, mixing entropy is 13.38 [J/ (mol. K)], which is equal to $1.61R$. In contrast, the mixing entropy of $CrCu_2Fe_2MnNi_2$ is 12.97 [J/ (mol. K)] which is equal to $1.56R$ or mixing entropy of $Cr_2Cu_2FeMn_2Ni_2$ is 13.14 [J/ (mol. K)] which is equal to $1.58R$. They are both slightly smaller than the mixing entropy of equiatomic CrCuFeMnNi [13].

Since the lower limit for HEAs is 1.5R, there is a need for further categorization to separate the alloy groups with mixing entropy difference lower than 1.5R. Low-entropy alloys (LEAs) and medium-entropy alloys (MEAs); in other words, traditional alloys, where 1R is the boundary between these two alloys are defined as in Equation 1.8 and Equation 1.9, respectively [3, 13]. To put it differently, alloys based on one principal element were classified by Yeh as LEAs, while MEAs consist of two to four principal elements as shown in Figure 1.2.

$$\Delta S_{conf} \leq R \tag{1.8}$$

$$R \leq \Delta S_{conf} \leq 1.5R \tag{1.9}$$

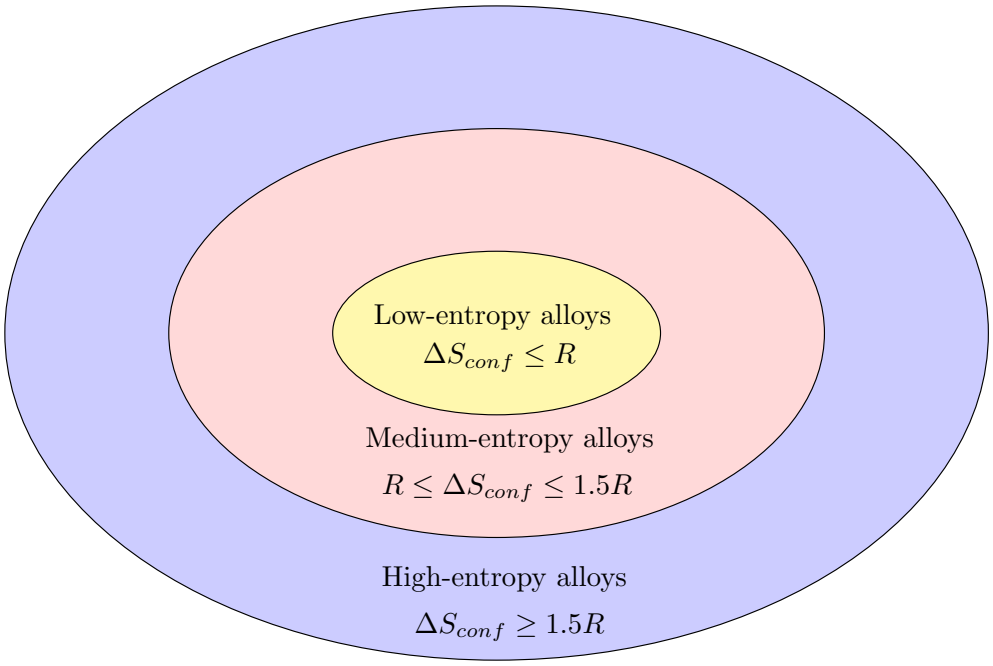

Figure 1.2 Classification of alloys in terms of configurational entropy range.

To sum up, HEAs are significant due to two related reasons. The first reason is to have high entropy which improves the quality of solid solution phases. The second reason is to prevent the formation of intermetallic compounds, such as crystalline or quasicrystalline, which are brittle by nature. If an alloy has these two properties, then it will have outstanding mechanical properties which notably contribute to the current body of scientific knowledge [3, 7, 13].

1.2 Core Effects of HEAs

Physical metallurgy studies the relationship between composition, manufacturing, lattice structure, physical and mechanical properties of materials [9, 10]. Because HEAs are quite different from traditional alloys in terms of the number of compositions, these principles might need to be altered. HEAs have unique properties which are combined in four core effects; high-entropy effect, sluggish diffusion effect, severe lattice distortion effect and cocktail effect. These effects have impacts on thermodynamics, kinetics, structure, and properties, respectively as shown in Figure 1.3.

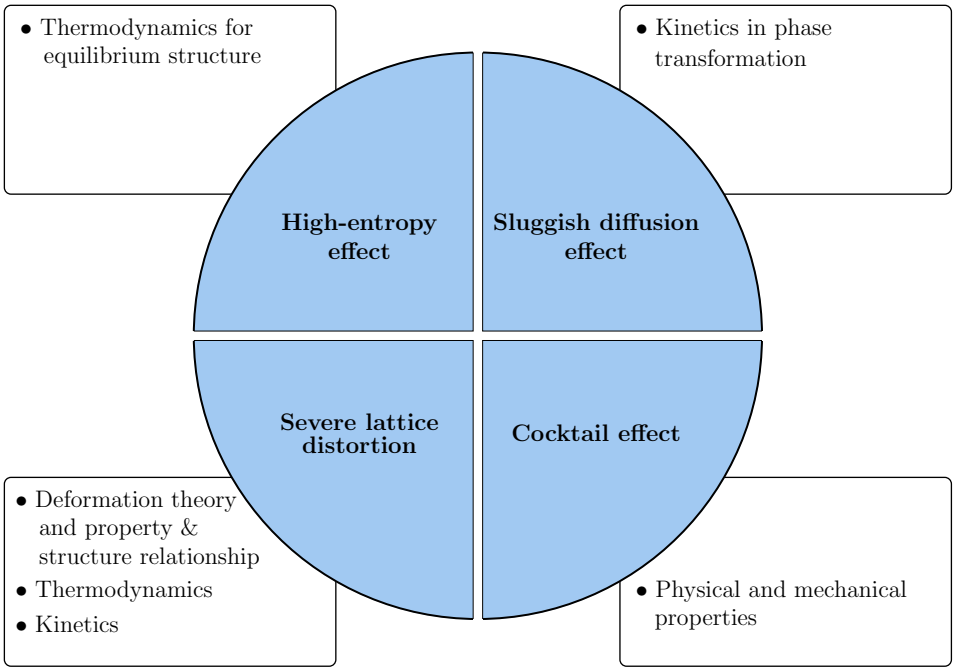

Figure 1.3 The scheme of four core effects of HEAs with impacts on physical metallurgy.

1.2.1 High-Entropy Effect

The high-entropy effect can be considered as the most important feature of HEAs. This effect is well known with enhancing the solid phase formation; therefore, it affects toughness by increasing strength and ductility. However, the reasons why high entropy improves the solution phase formation were not clear until Yeh explained in [3]. Some technical background needs to be mentioned before starting to explain reasons behind high-entropy effect.

There are three possible groups to finalize an alloy's solid state: elemental phases, intermetallic compounds, and solid solution phases [3]. Elemental phase is based on one metallic element, while the intermetallic compound consists of special superlattices.

Lastly, solid solution phases can be categorized into two groups, random and ordered solid solutions. When the atoms of solute are present in the lattice of the solvent, the solid solution is formed. The crystal structure of the solvent remains unchanged by the addition of the solutes. An ordered solid solution, or intermetallic phase, is a solid solution in which atoms arrange themselves in a regular or a preferential position in the lattice such as Ba_2Pt. For a random solid solution, atoms from different components arrange their positions in lattice sites by probability. FCC, BCC and HCP are common examples of the random solid solution.

From thermodynamics, a system reaches equilibrium state when the Gibbs free energy attains the lowest at given T and P. If we recall Equation 1.1 and think of all parameters that affect Gibbs free energy, we can compare all types of solid states in terms of their Gibbs free energy in Table 1.2. The values in Table 1.2 are approximate values, and they do not contain any strain energy contribution to mixing enthalpy due to atomic size differences.

Table 1.2 Comparisons of elemental phases, intermetallic compounds, partially ordered and random solid solutions in terms of ΔG_{mix}, ΔH_{mix} and $-T\Delta S_{mix}$.

	Elemental Phases	**Intermetallic Compounds**	**Partially Ordered Solid Solutions**	**Random Solid Solutions**
ΔH_{mix}	Small negative	Large negative	Medium negative	Medium negative
$-T\Delta S_{mix}$	Small negative	Small negative	$< -RT\ln(n)$	$-RT\ln(n)$
$= \Delta G_{mix}$	Small negative	Large negative	Large negative	Large negative

As can be seen from Table 1.2, the random solid solution group includes HEAs. Although initially solid solutions have medium negative enthalpy, at the end, solid solutions finalize solid state with large negative Gibbs free energy due to contribution of large negative entropy. For all groups, it is hard to calculate the exact value of each parameter except for mixing entropy of multi-principal elements. Mixing entropy is often replaced by configurational entropy, which is the parameter that can be calculated easily. Therefore, even mixing entropy reflects approximate values. To sum up, rather than knowing the exact values, they are only comparable through groups. It is known that all kind of multi-principal elements can be thought of as solid solutions, and HEAs are inside this group. Therefore, this brings up the question why HEAs have medium mixing enthalpy, while intermetallic compounds have large mixing enthalpy. It is due to the number of bonds which affects mixing enthalpy directly. For example, one mole of NiAl intermetallic phase

(B_2) has (½)x8xN_o bonds, whereas the same compound, NiAl, in random solution would have half as many intermetallic phase bonds, which is equal to (½)x(½)x8xN_o. Therefore, the mixing enthalpy of ordered solid solution is twice that of random solid solution.

1.2.2 Severe Lattice Distortion Effect

Solid solution phases of HEAs are usually thought of as the whole matrix even if its structure is partially ordered such as FCC, BCC, HCP or other more complex structures due to the first effect of HEAs, high-entropy effect [5]. Since atoms in the matrix are surrounded by unlike atoms having different atomic sizes, each multi-principal alloy suffers from the lattice strain and stress represented in Figure 1.4. Different bonding energies and crystal structures also make tension and compression forces through whole-solute matrix even worse. In contrast, for traditional alloys, lattice distortion value is considerably smaller than that of HEAs, because of the possibility of having a same sort of atoms as neighbors [2-7, 10, 12-14].

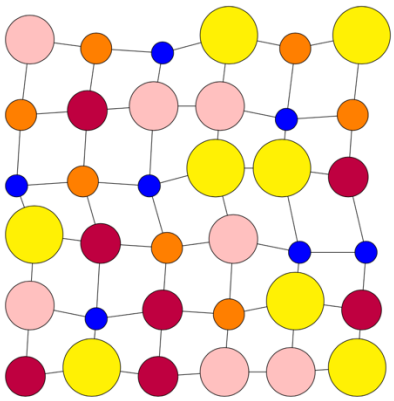

Figure 1.4 A schematic diagram indicating a severely distorted matrix of a solid solution with five different components in two-dimension.

A well-known approach to describe the lattice distortion is consideration of atomic size differences, which can be thought of as only parameter [8, 15, 16]. There is a direct relationship between the lattice distortion and the difference in atomic size (δ) given in Equation 1.10 where c_i, r_i and $\bar{r}$ are the atomic percentage, the atomic radius of the i-th element and the average atomic radius, respectively.

$$\delta = 100 \sqrt{\sum_{i=1}^{n} c_i \left(1 - \frac{r_i}{\bar{r}}\right)^2} \tag{1.10}$$

$$\bar{r} = \sum_{i=1}^{n} c_i r_i$$

Although this is the most common way to describe the lattice distortion, there are some drawbacks. First, Equation 1.10 is valid for pseudo-unary matrix systems. However, with some assumptions, this equation was used for multi-component matrix. The second drawback is that this approach only covers the effects of the atomic size differences on the lattice distortion; therefore, not only is the different bonding energy neglected, but also the different crystal structure tendencies are neglected.

Severe lattice distortion can affect some properties of a material such as hardness, strength, electrical and thermal conductivity. Hardness and strength increase with the lattice distortion, which in turn, is caused by solution hardening. For instance, for the equiatomic CoCrFeMnNi HEA, Vickers hardness test results show that a homogenized sample has a higher hardness value (1192 MPa) than the one obtained by the mixture rules (864 MPa) [17]. In the same paper, Senkov also studied on MoNbTaVW which has BCC lattice

structure, and its Vickers hardness result is 5250 MPa. He concluded that BCC alloys have higher hardness values than alloys with FCC lattice structure. This might be because FCC lattice has twelve nearest neighbor atoms, whereas BCC lattice only has eight nearest neighbor atoms.

On the other hand, electrical and thermal conductivity sharply decrease as severe lattice distortion increases [4, 18, 19]. In 2007, Yeh studied X-ray diffraction on HEAs, and he stated that because of the diffuse scattering on the severely distorted surface, the intensity of the peak sharply decreases compared with others [4]. In [18], Kao et al. contributed to Yeh's studies and focused on physics behind the HEAs, especially electrical, magnetic and thermal behavior of HEAs. Kao stated that the lattice distortion causes electron scattering, which results in a remarkable drop in electrical conductivity. In the following years, thermal conductivity and thermal diffusivities of HEAs were studied, and it was pointed out that thermal diffusivities of HEAs also decrease with the lattice strain and stress. Thermal diffusivities of four different HEAs and pure Al were expressed as a function of temperature. Thermal diffusivity of pure Al is quite sensitive to temperature differences, while four HEAs samples are not [19]. The reason why HEAs have a relatively small temperature coefficient of resistance than traditional alloys or pure elements is that the lattice distortion generated by thermal vibrations is negligible in comparison with the severe lattice distortion [4].

1.2.3 Sluggish Diffusion Effect

The sluggish diffusion effect is related to phase transformation and diffusion. A phase transformation caused by diffusion in HEAs is slower compared to conventional alloys. Before understanding the reasons behind this effect, it is necessary to know some concepts about diffusion and the vacancy effect in thermodynamics. A vacancy is one of the point defects which is a zero-dimensional imperfection in the crystal. Vacancies cause a distortion of planes which means excess elastic energy in the lattice so the internal energy increases, hence; the enthalpy of the whole system also increases. Therefore, Gibbs free energy is supposed to increase; yet Gibbs free energy is smaller for a certain concentration of point defect at a given temperature. Thus, the number of vacancies in the crystal will seek the value that makes Gibbs free energy a minimum at any given temperature. It is due to the fact that the increase in the entropy outweighs the increase in enthalpy [11]. The relation between the vacancy and the activation energy at a given temperature is as shown below.

$$\frac{N_D}{N} = e^{\frac{-Q_D}{kT}}$$

Here N_D, N, Q_D, k and T denote the number of vacancies, the number of atoms in the crystal, the activation energy, the Boltzmann's constant and temperature, respectively.

For the first time, in 2013, Tsai et al. studied [20] the sluggish diffusion effect of HEAs to prove indirect evidence. The authors used three diffusion couples and six different alloy

systems in diffusion experiments to calculate temperature dependence of the diffusion coefficient for some transition elements.

Various researchers working on HEAs indicated that sluggish diffusion has some advantages on HEAs' microstructure and mechanical properties [5, 6, 14, 21-30]. For example, increased recrystallization temperature, slower grain growth, increased creep resistance, toughness and strength are just a few of them. In [23], Liu showed how improved grain structure affects mechanical behavior of CoCrFeMnNi HEAs with FCC phase due to sluggish diffusion effect.

1.2.4 Cocktail Effect

In 2003, the term 'cocktail effect' was first used by Ranganathan in [31] for HEAs although conventional alloys also have this property. HEAs can be single-phase or multi-phase consisting of at least five elements; therefore, the cocktail effect plays an important role in HEAs' design. The cocktail effect can be thought of as a composite effect. To illustrate that, if more light elements are used such as Al, the overall density of an alloy will decrease. There are two different studies conducted about the cocktail effect on HEAs. The first study was conducted by Yeh in 2006. The $Al_xCrCoCuNiFe$ HEAs with various Al content (between 0-43 atomic percentage) were prepared by vacuum-arc melting technique, and Table 1.3 shows how hardness and phase of the $Al_xCrCoCuNiFe$ HEA change with an addition of Al element.

Table 1.3 Contributions of the cocktail effect on $Al_xCrCoCuNiFe$ alloys in terms of hardness.

Al content (at .%)	Hardness (Hv)	Phase
Between 0-15	Between 125-350	FCC
Between 15-35	Between 350-650	FCC + BCC
Between 35-43	Between 650-670	BCC

Another study was conducted by Senkov, and he showed the differences in mechanical behavior between two different refractory HEAs with BCC structure, which are the quinary near-equiatomic VNbMoTaW alloy and the quaternary near-equiatomic NbMoTaW alloy. As can be seen from Figure 1.5, both compression samples have the remarkable plastic strain at 600 °C and above, yet both samples experienced about %30 drop in yield strength between room temperature and 600 °C. For the near-equiatomic NbMoTaW alloy, the yield strength at room temperature, the maximum strength and Young's modulus are 1058 MPa, 1211 MPa and 220 ± 20 GPa, respectively, while the near-equiatomic VNbMoTaW alloy at the same temperature shows the yield point at 1246 MPa and the maximum stress strength 1270 MPA with 180 ± 15 GPa Young's modulus.

On the other hand, the NbMoTaW alloy at 1200 °C flows the near-steady state condition, while VNbMoTaW experiences considerable softening after yielding [28].

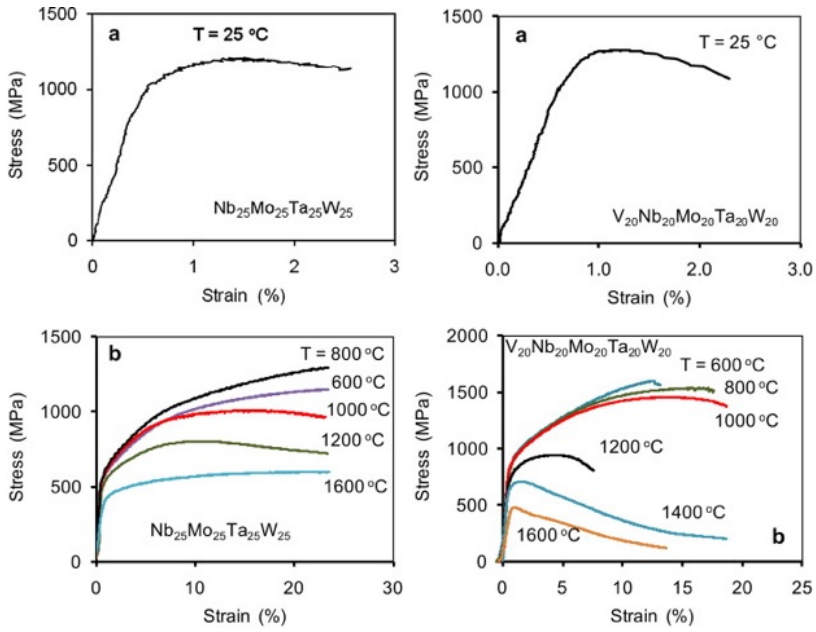

Figure 1.5 Compressive engineering stress-strain curves of quaternary near-equimolar NbMoTaW and quinary near-equiatomic VNbMoTaW (a) at room temperature and (b) at various temperatures between 600 °C and 1600 °C. Reprinted with permission from [28].

To understand cocktail effect in depth, I will show different superalloys that were studied in [28]. Figure 1.6 indicates the temperature dependence of the yield stress of NbMoTaW, VNbMoTaW and two other superalloys which are Inconel 718 and Haynes 230. As can be seen from Figure 1.6, even at elevated temperatures such as 1600 °C, two HEA samples resist to softening and complete the experiments above 400 MPa, whereas other

superalloys could not achieve to reach at this value. The reason behind this impressive mechanical behavior is that, for NbMoTaW and VNbMoTaW HEAs, all constituent elements are selected from refractory elements. As a result, melting points of NbMoTaW and VNbMoTaW HEAs are above 2600 degrees due to cocktail effect. In addition to cocktail effect, these results are also explained with the sluggish diffusion effect at elevated temperatures [17, 28].

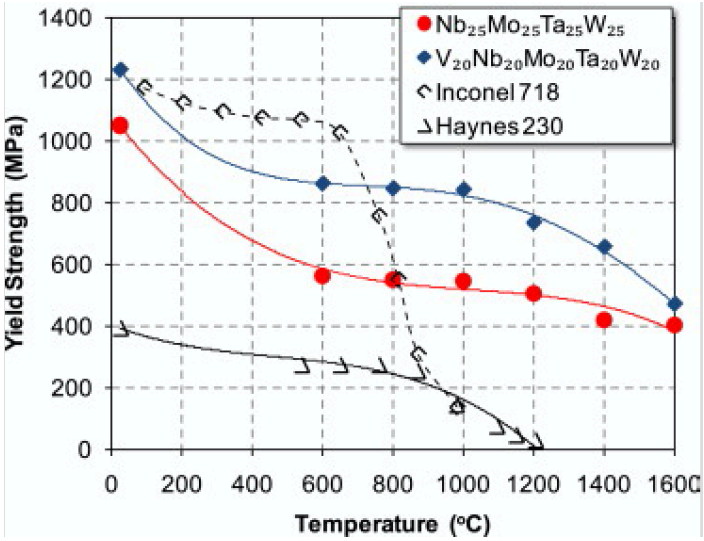

Figure 1.6 Yield strength of NbMoTaW, VNbMoTaW and two superalloys as a function of temperature. Reprinted with permission from [28].

1.3 Previous Studies on CoCrFeMnNi High-Entropy Alloy

Numerous HEAs have been developed because they have a favorable combination of outstanding mechanical and thermal properties such as strength, toughness, corrosion

resistance and thermal-stability. The composition is a unique factor in order to determine crystallographic features, microstructure, and thus all characteristic properties. CoCrFeMnNi is one of the most common and fundamental quinary HEAs. Using transition metals, such as Co, Cr, Fe, Mn and Ni in an alloy, are important for high-temperature load-bearing structures and thermal systems. In addition to composition, concentration of these atoms in an alloy is also important for characteristic properties. Their presence in an equiatomic concentration allows an alloy to have maximum configurational entropy. As a result, many researchers have tended to study equiatomic CoCrFeMnNi.

The equiatomic FCC-structured CoCrFeMnNi HEA was first reported by Cantor in 2004 [1]. Several equiatomic HEAs containing components up to 20 have been fabricated. Some alloys, such as the ones with 16 and 20 components, are multi-phase which result in brittle mechanical properties in nature. Cantor explained the reason why some alloys are predominantly a single FCC phase is because they contain high atomic percentage in transition metals. It has also been concluded that with an addition of Cu, Ge and Nb to CoCrFeMnNi individually has not change FCC phase, yet adding more electronegative components results in incredibly less solubility. Figure 1.7 shows that all the alloys have a dendritic structure, yet the size and morphology alter for each alloy [1].

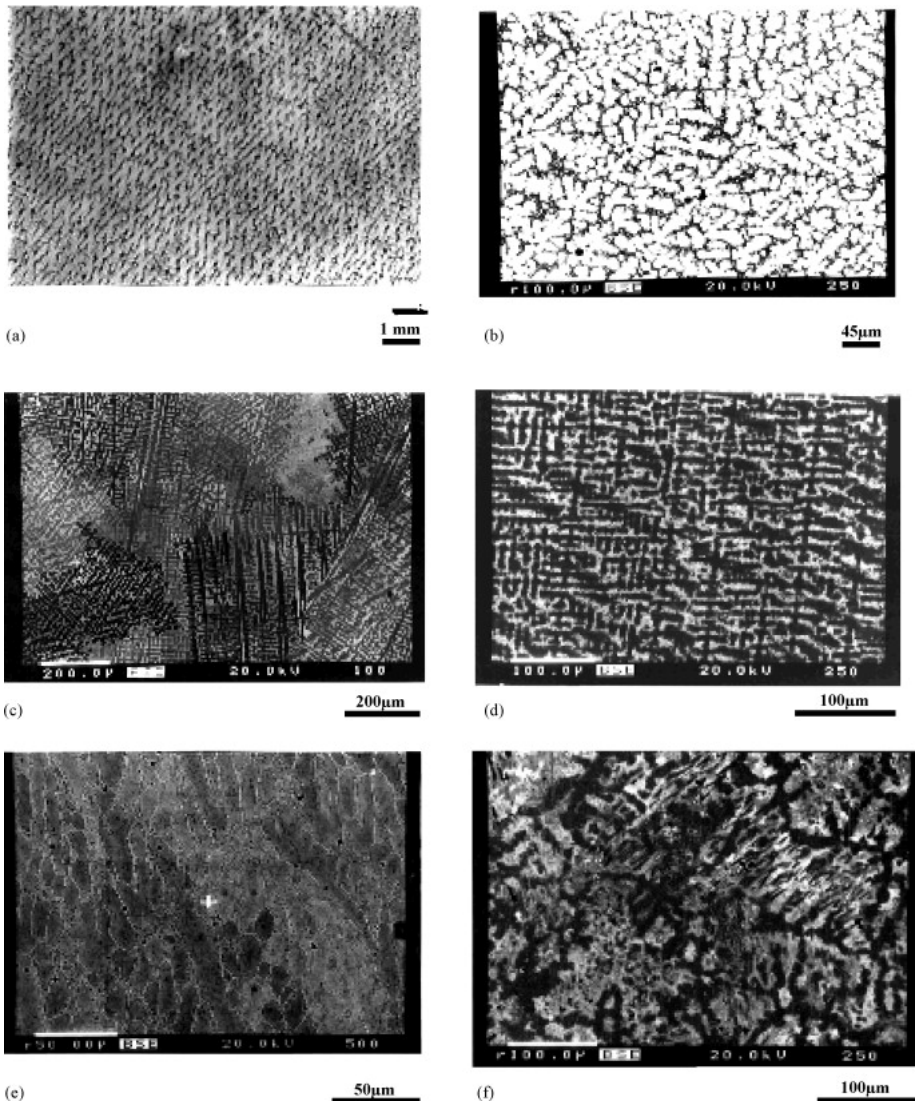

Figure 1.7 (a) Optical images of equimolar CoCrFeMnNi and SEM images of equimolar (b) FeCrMnNiCoNb; (c) FeCrMnNiCoGe; (d) FeCrMnNiCoCu; (e) FeCrMnNiCoTi; (f) FeCrMnNiCoV. Reprinted with permission from [1].

Instead of comparing properties of the equimolar quinary and the sexinary HEAs as in [1], Gali researched the tensile properties of the equiatomic CoCrFeMnNi HEA and the CoCrFeNi MEA, which were manufactured by arc melting, drop casting and hot rolling

[32]. Backscattered electron images were obtained, and Figure 1.8 shows that equimolar CoCrFeMnNi contains isolated dark particles, which were manganese oxide or/and chromium oxide detected with X-ray. On the other hand, these dark particles were not present in equimolar CoCrFeNi. The author did not explain the reason why CoCrFeMnNi has oxygen contamination and CoCrFeNi does not. The melting point ranges of CoCrFeMnNi and CoCrFeNi were also determined to be 1280 -1349 °C and 1422-1462 °C. As can be seen in Figure 1.8, CoCrFeMnNi has three times larger grains than CoCrFeNi (32μm and 11μm) after hot rolling at 1000 °C. The larger grain size was explained by the higher homologous temperature of CoCrFeMnNi (~0.81 T_m).

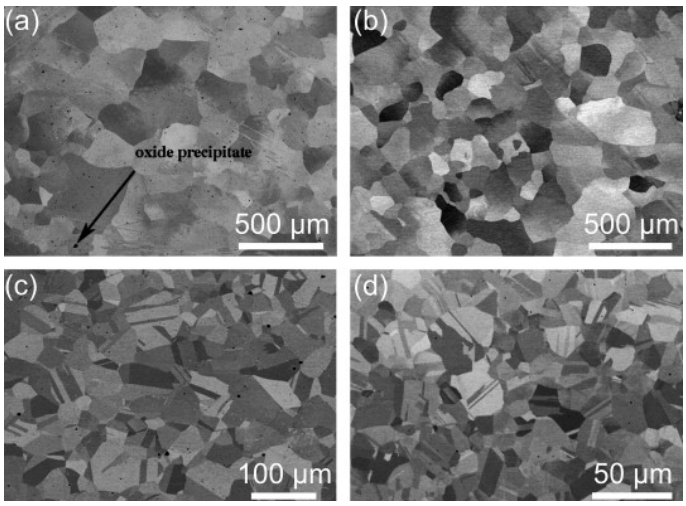

Figure 1.8 Backscattered electron images of as-cast and homogenized (a) CoCrFeMnNi (b) CoCrFeNi and hot-rolled (c) CoCrFeMnNi (d) CoCrFeNi. Reprinted with permission from [32].

Tension tests with two sample sets for each alloy were performed at various temperatures with different strains. It was observed that these two alloys have a strong temperature dependence yet a weak strain rate dependence. Figure 1.9 shows a comparison of the yield stress and the ultimate tensile stress of CoCrFeMnNi HEA and CoCrFeNi MEA with a wide range of temperature differences. As can be seen in Figure 1.9, the difference between the yield stress and ultimate tensile stress (strain hardening) at a low temperature was expressed as a considerable work hardening effect. The reason behind the existence of significant work hardening at a low temperature is due to mechanical twinning mechanisms. The yield stress and the ultimate tensile stress showed the same tendency across increased temperatures; they decreased sharply when the temperature increased [32].

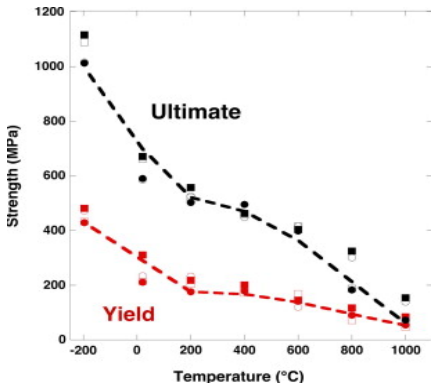

Figure 1.9 The yield stress and the ultimate tensile stress of CoCrFeMnNi HEA and CoCrFeNi MEA as a function of temperature range between -196 °C and 1000 °C. The circles and squares represent CoCrFeMnNi and CoCrFeNi, respectively; for each, the filled symbols for 10^{-3} s^{-1} and open symbols are 10^{-1} s^{-1}. Reprinted with permission from [32].

Unexpectedly, strength and ductility are not mutually exclusive like many conventional materials. Ductility and strength have the same tendency through increment in temperature. They both decrease with increasing temperature as shown in Figure 1.10 (a) [32]. In Figure 1.10 (b) and (c), there is almost no necking at -196 °C for CoCrFeMnNi tension fracture sample, whereas this is not the case at 400 °C. The large elongation in Figure 1.10 (b) was explained with necking instability being postponed to a higher strain. Microvoids, or dimple rupture, in the interior of the sample can be seen in Figure 1.10 (c) at the fracture point, which is an indicator of a ductile material. In Figure 1.10 (e), there is a remarkable necking at high temperatures and lower ductility at a higher temperature. It can be associated with the earlier onset of the necking, which explains the lower work hardening at elevated temperatures.

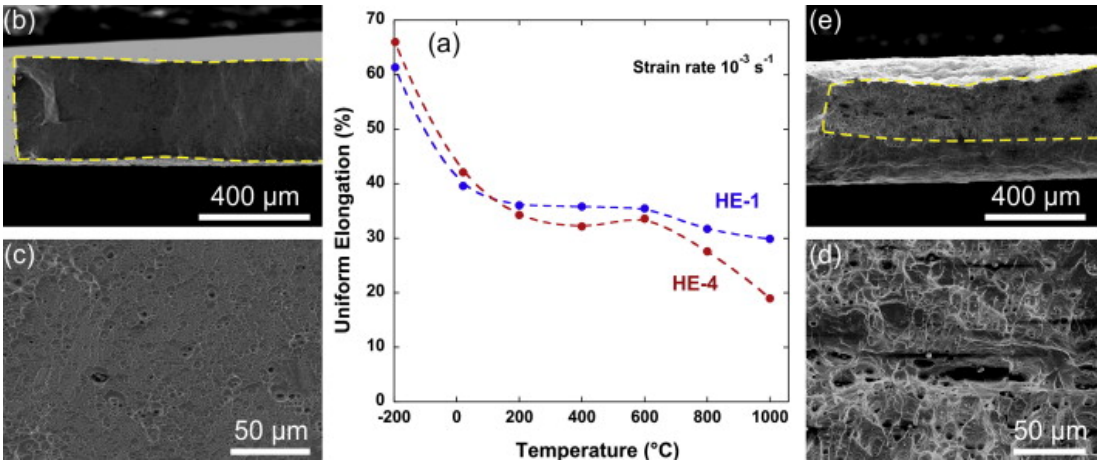

Figure 1.10 (a) Ductility of the CoCrFeMnNi HEA and the CoCrFeNi MEA as a function of temperature, (b, c) are images of the CoCrFeMnNi tension specimen at -196 °C and (d, e) at 400 °C. Reprinted with permission from [32].

1.4 Principle of Equal Channel Angular Extrusion

Nanostructured and ultra-fine grained materials have grabbed researchers' attention due to their remarkable enhanced mechanical and physical properties [33, 34]. There are numerous techniques used to fabricate nanostructured and ultra-fine grained materials [34, 35]. Severe plastic deformation (SPD) technique is just one of them. SPD techniques have a lot of advantages over others. To name a few, with SPD techniques, very high strains can be achieved at relatively low temperatures in order to form nanostructured materials. Moreover, traditional techniques can result in a cellular type microstructure with low angle grain boundaries, while SPD techniques may reduce grain sizes from 1 mm to 100-200 nm with high angle grain boundaries.

In this study, we focus on one of the SPD techniques, which is called the equal channel angular extrusion (ECAE) process. The idea behind the ECAE process is to develop a simple shear, and it was introduced by Vladimir Segal [36, 37]. The ECAE method is performed by putting a ceramic-glazed billet into a lubricated die, which consists of two integrated channels with an equal cross-section area. This process is described in Figure 1.11. There are two essential assumptions for this process. The first one is that plastic flow occurs under steady-state conditions, which means that plastic flow is not a function of time. The second assumption is that shear deformation occurs in two dimensions, not in three dimensions. It enables us to predict and interpret results more easily than three-dimensional shear deformation.

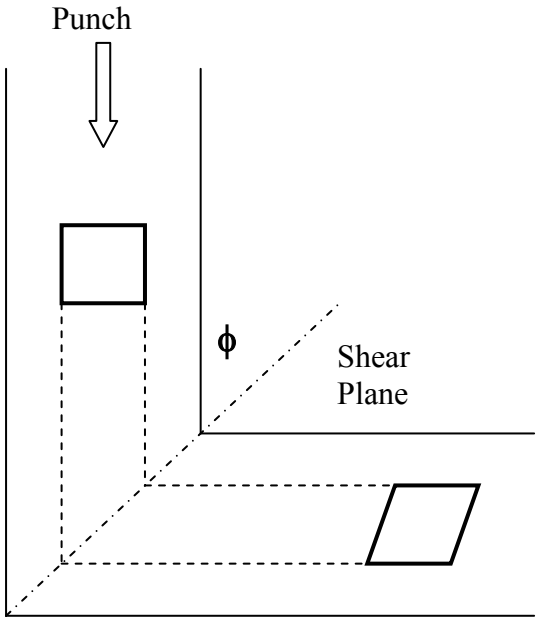

Figure 1.11 A schematic diagram of an ECAE die and a heavily deformed uniform microstructure representation.

The angle between the two integrated channels is denoted by 2Ø. Simple shear achieves deformation at the crossing plane of the channels. Before and after the crossing plane, we assume the billet motion is rigid body motions, which means that the distance between any two points inside the billet does not change permanently. In other words, the surfaces of the channel and billets create some friction force that affects billet motion, but we neglect all kinds of frictions and deformations except for the crossing plane [34, 36]. The billet moves forward along the die with the same uniform manner, except for the small end regions and minor surface areas of the billet. The relationship between strain and the ECAE die geometric parameter, which is a half of the angle between two channels, Ø, per pass for the processed billet, is shown below [36, 38].

$$\varepsilon = \frac{2}{\sqrt{3}} \times \cot \emptyset$$

The ECAE process can be repeated several times to reach the desired deformation, which increases proportionally with the number of passes and initial strain [38].

$$\varepsilon_t = N \times \varepsilon$$

Here ε is the initial Von Misses strain, ε_t is the final strain, and N is the number of passes. The critical punch pressure ($P_{critical}$) which is required to press bulk billet can be expressed as below.

$$P_{critical} = \frac{2}{\sqrt{3}} \times \sigma_y \times \cot \emptyset$$

Here σ_y is the initial yield stress of the material. To calculate the equivalent area reduction (AR), first, the reduction ratio (RR) is required, the formulas for which are as shown below.

$$RR = e^{N \times \varepsilon}$$

$$AR\ (\%) = \left(1 - \frac{1}{RR}\right) \times 100\%$$

In this study, the die angle, 2Ø, is equal to 90º. By the help of servo hydraulic punch, the billets can be pressed several times through the channels. Some significant variables depending on a 90º die and the number of passes are shown in Table 1.4. These parameters are calculated up to N=4.

Table 1.4 Some important calculated ECAE parameters affecting mechanical behavior up to N=4. This table is valid for Ø=45º.

Number of Passes	Total Strain	Equivalent Reduction Ratio	Equivalent Area Reduction (%)
N=1	1.15	3.2	69
N=2	2.31	10.1	90
N=3	3.46	31.82	97
N=4	4.62	101	99

There are several routes to complete the ECAE process, and just a few of them, which are conducted in and related to this research, are discussed. Figure 1.12 describes some ECAE routes schematically.

Table 1.5 Some routes of the ECAE process and their dependent variables.

Route	Minimum number of passes	Billet rotation about the extrusion axis				Effects on microstructures
		$1 \rightarrow 2$	$2 \rightarrow 3$	$3 \rightarrow 4$	$4 \rightarrow N$	
A	1	0°	0°	0°	etc.	Lamellar elongation
B	2	+90°	−90°	+90°	etc.	Filamentary elongation
C	2	+180°	+180°	+180°	etc.	Back and forth shearing
C'	4	+90°	+90°	+90°	etc.	Back and forth cross-shearing
E	4	+180°	+90°	+180°	etc.	Back and forth cross-shearing

Table 1.5 shows the summary of routes and other parameters. In Route A, each pass the billet keeps its original position, which means there is no rotation between passes about the extrusion axis. Therefore, when the number of passes increases, the microstructure of the billet is becoming more and more elongated due to distortion in the same direction.

In Route B, two directions (+90º / -90º) are chosen about the extrusion axis. The billet in each odd numbered pass (N= 3, 5, etc.) is rotated -90º from the previous position, and in each even numbered pass (N=2, 4, etc.) is rotated +90º from the previous location. The first pass is called N=1, so billet at N=1 can be extruded in any positions. The rest will depend on the first pass position. Therefore, after each completed odd-numbered passes, the billet comes to its unprocessed position. After the ECAE process in Route B, the microstructure of the billet is neither lamellar like Route A when N=2, 3, etc. nor equiaxed like Route C when N=2,4, etc. Filamentary type grains are fabricated during Route B after even-numbered passes are completed. Route B is one of the three-dimensional deformations.

In Route C, after each pass, the billet is rotated +180º around its extrusion axis. After each odd-numbered pass, the billet is deformed, and after each even-numbered pass, the microstructure of the billet is restored to its near-original grain shape. Similar to Route A, Route C is also a two-dimensional deformation.

The only difference between Route C and Route C' is the rotation degree. Instead of +180º in Route C', the rotation after each pass is +90º. Likewise Route B, Route C' is also three-dimensional deformation.

Route E is a kind of combination of Route C and C'. At even-numbered passes, the billet is rotated +180º around the axis and at odd-numbered passes, +90º. The grain size refinement is better than Route C.

In this study, we used the combination of the original routes for each billet. Also, to observe the differences in the microstructure, we tried to use different routes over four billets. In Chapter 2, which routes were chosen and combined will be discussed in detail.

1.5 Motivation

A composition of an alloy is the unique factor to determine crystallographic features, microstructure, and thus all characteristic properties of an alloy. CoCrFeMnNi is one of the most common and fundamental quinary HEAs. Although in [2-7, 13] Yeh claimed that high mixing entropy is sufficient to predict whether or not an equiatomic alloy will form a stable single-phase solid solution, Otto pointed out that it is not the only factor and disproved Yeh's hypothesis [27]. By replacing a component of CoCrFeMnNi with other transition metal elements, five different alloys were produced in equimolar condition such as TiCrFeMnNi, CoVFeMnNi, CoMoFeMnNi, CoCrVMnNi, CoCrFeMnCu. The replaced elements were chosen due to the same crystal structure at room temperature and the similar electronegativity (EN) of the elements being replaced to retain configurational entropy. Equimolar CoCrFeMnNi was proven as stable single-phase HEA by Cantor [1]. Then, CoCrFeMnNi were fabricated to investigate similarities with and differences from other five alloys. Based on Otto's calculations, the best candidate for single-phase solid solutions is CoCrFeMnCu due to its lowest average EN and metallic radius (r_{atom}) values among other five alloys. After solidification, their microstructures are as shown in Figure 1.12. As Cantor studied [1], Otto also proved that CoCrFeMnNi has a stable single FCC phase shown in Figure 1.12 (a). As shown in Figure 1.12 (b), the best candidate, CoCrFeMnCu, did not show stable single-phase like other four alloys [27] despite what

Yeh predicted in [2-6]. Experimentally proven results in two separate studies about phase stability are one of the reasons why CoCrFeMnNi will be chosen as a material for this proposed work. A stable phase is important and is required for the desired physical property of high-temperature load-bearing structures and thermal systems.

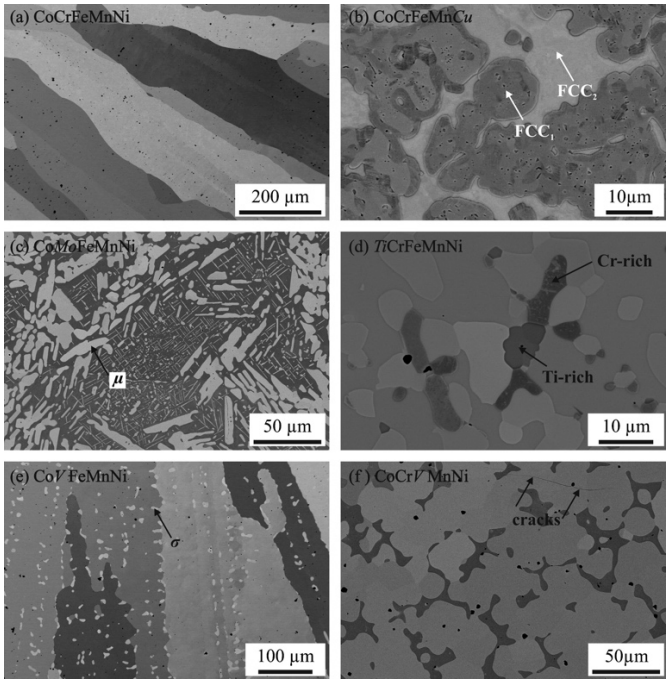

Figure 1.12 Backscatter electron (BSE) images of six manufactured alloys. Reprinted with permission from [27].

The concentration of atoms in an alloy is also important for characteristic properties of materials. Being present in equiatomic concentration allows an alloy to have maximum configurational entropy. Therefore, in this research, near-equimolar CoCrFeMnNi alloy will be investigated due to the notable reasons mentioned above.

As mentioned in Section 1.4, nanocrystalline and ultra-fine grained materials have been attractive due to their enhanced physical and mechanical properties. There are several techniques to fabricate ultra-fine grained materials. Severe plastic deformation (SPD) is the most popular technique due to its applicability and feasibility to the industry. One of SPD techniques, the ECAE process, benefits from shear stress to obtain heavily deformed microstructure.

There are numerous remarkable reasons to use the ECAE process. The first reason is to create uniform and simple shear through billet which is important for near-ideal deformation [36, 37, 39]. In addition to uniform strain distribution, without any changes in a cross-section area of billet, uniform deformation can be obtained even at low pressure and force. Also, the process can be repeated several times to reach the desired deformation, which increases proportionally with the number of passes and the initial strain [38]. In [23, 26, 32, 40, 41], with different SPD techniques, grain size effects of HEAs on mechanical behavior were investigated. Nevertheless, none of the researchers examined the mechanical behaviors of the ECAE processed CoCrFeMnNi. In [41], Yoshida showed how a grain size affects the tensile stress behavior for MEA which can be observed in Figure 1.13. As seen in Figure 1.13, the yielding stress increases enormously with decreasing the grain size. In addition to stress-strain curve, with Hall-Petch plot, the relationship between grain size of the alloy and mechanical strength is obvious. Compared with pure Ni and Ni-40Co, the slope of CoCrNi MEA is highly greater.

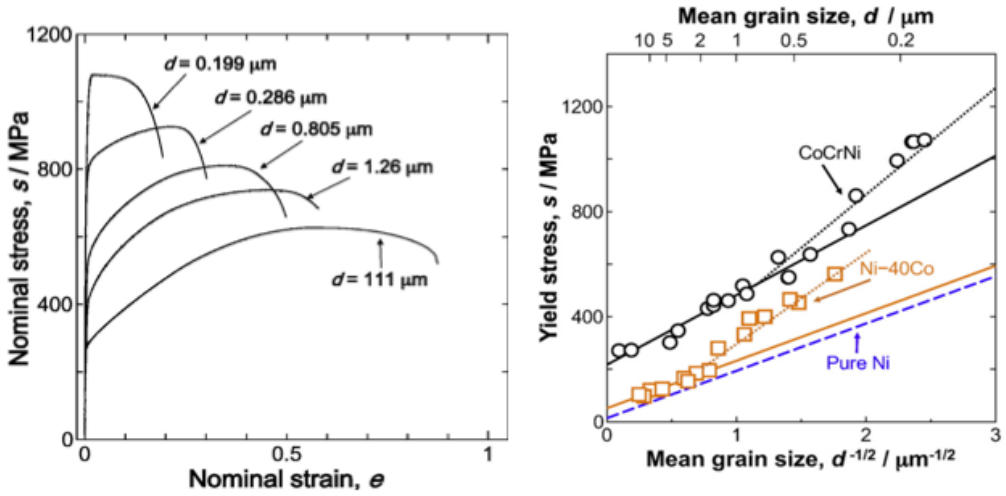

Figure 1.13 Grain size effects on engineering stress-strain curves and Hall-Petch plot of CoCrNi MEA. Reprinted with permission from [41].

In this research, the effects of the ECAE method on the mechanical properties of equiatomic CoCrFeMnNi HEA were investigated in detail. The aims were to increase the dislocation density and to obtain the submicron grain size. Therefore, the effect of the increased dislocation density and the submicron grain size on the mechanical properties of CoCrFeMnNi were also assessed by performing tension tests.

The specific tasks of the current study are outlined as follows:

1) Conducting the ECAE process on the as-cast CoCrFeMnNi HEA.
2) Investigating the microstructure evaluation during the ECAE process under different conditions via the Secondary Electron Microscopy (SEM) and the Backscattered Electron (BSE) images.

3) Comparing the microstructures of the as-cast and the as-processed ECAE samples.
4) Pointing out the mechanical properties of extruded billets at room temperature with tension and Vickers hardness tests.
5) Correlating the mechanical properties with the created microstructures after the ECAE process.

CHAPTER II

EXPERIMENTAL METHODS

Near-equimolar quinary CoCrFeMnNi HEA was supplied from the company called Sophisticated Alloys in the form of a cylindrical rod with 1.25-inch diameter and 20-inch length. The alloy had a composition of 23.01% Co, 16.98% Cr, 19.79% Fe, 18.85% Mn, 21.37% Ni and was fabricated by the vacuum induction melting technique under the Argon backfill. The melt chamber was evacuated to 1 x 10^{-4} Torr and then it was filled back with Argon to 100 Torr before induction heating. The alloy was melted in an Alumina crucible and was poured in a Graphite mold, which was coated with a Zirconia wash. This was followed by hot isostatic pressing at 15 Ksi and 2200 °F for 4 hours followed by furnace cooling.

2.1 As-Cast Condition of the Material

Examination of the as-received material was important to compare the results of the as-processed material. Before the ECAE process, the as-cast material was investigated with EDS and SEM. Figure 2.1 shows the EDS images of the as-received material. Even though we had the metal chemistry results that was sent by the company, we wanted to make sure whether or not the as-received metal was near-equiatomic CoCrFeMnNi. Another reason to perform EDS test was to investigate the effect of porosity on the material. Frequently, we observed black cumulative dots which means that they were oxide or porosity. With EDS results, we deduced that they were not oxide particles. Table 2.1 shows the nominal composition and the composition of EDS results.

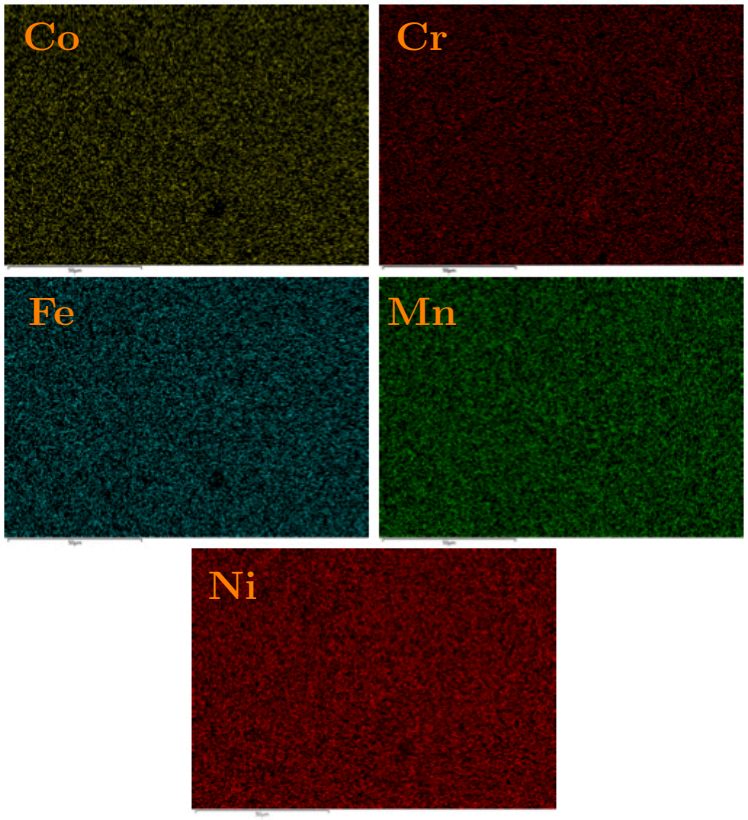

Figure 2.1 EDS results of the as-received material.

Table 2.1 The comparison of the nominal composition and the composition of EDS results.

Nominal Composition (at%)				
Co	**Cr**	**Fe**	**Mn**	**Ni**
23.01	16.98	19.79	18.85	21.37
Composition of EDS Results (at%)				
Co	**Cr**	**Fe**	**Mn**	**Ni**
22.13	17.59	19.68	18.97	21.63

Secondly, the SEM study was conducted to calculate the initial grain size and to observe the microstructure of as-cast materials. This was important because we needed to compare a mean grain size of the material before and after the ECAE process. Therefore, knowing the grain size of the material was a good indicator to correlate the mechanical behaviors and the microstructure of the materials. In addition, the SEM study was a good way to see the as-cast porosity condition. As seen in Figure 2.2, in some places a few porosity clusters were observed, and in general uniformly distributed porosity and small voids inside the material were defined. After the ECAE process, we claimed that these porosities would close down. In Chapter 3, the porosity and its effects on the mechanical behavior after the ECAE process will be discussed in detail.

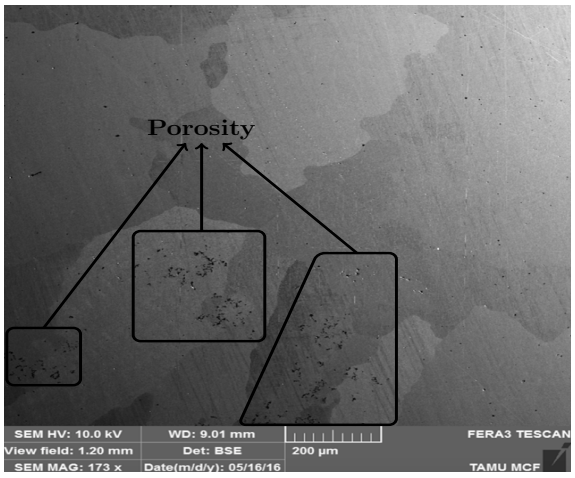

Figure 2.2 Porosity clusters inside the as-received material.

Figure 2.3 shows the BSE images of the as-received material which had very large coarse grains with a mean grain size of 200 ± 118 µm.

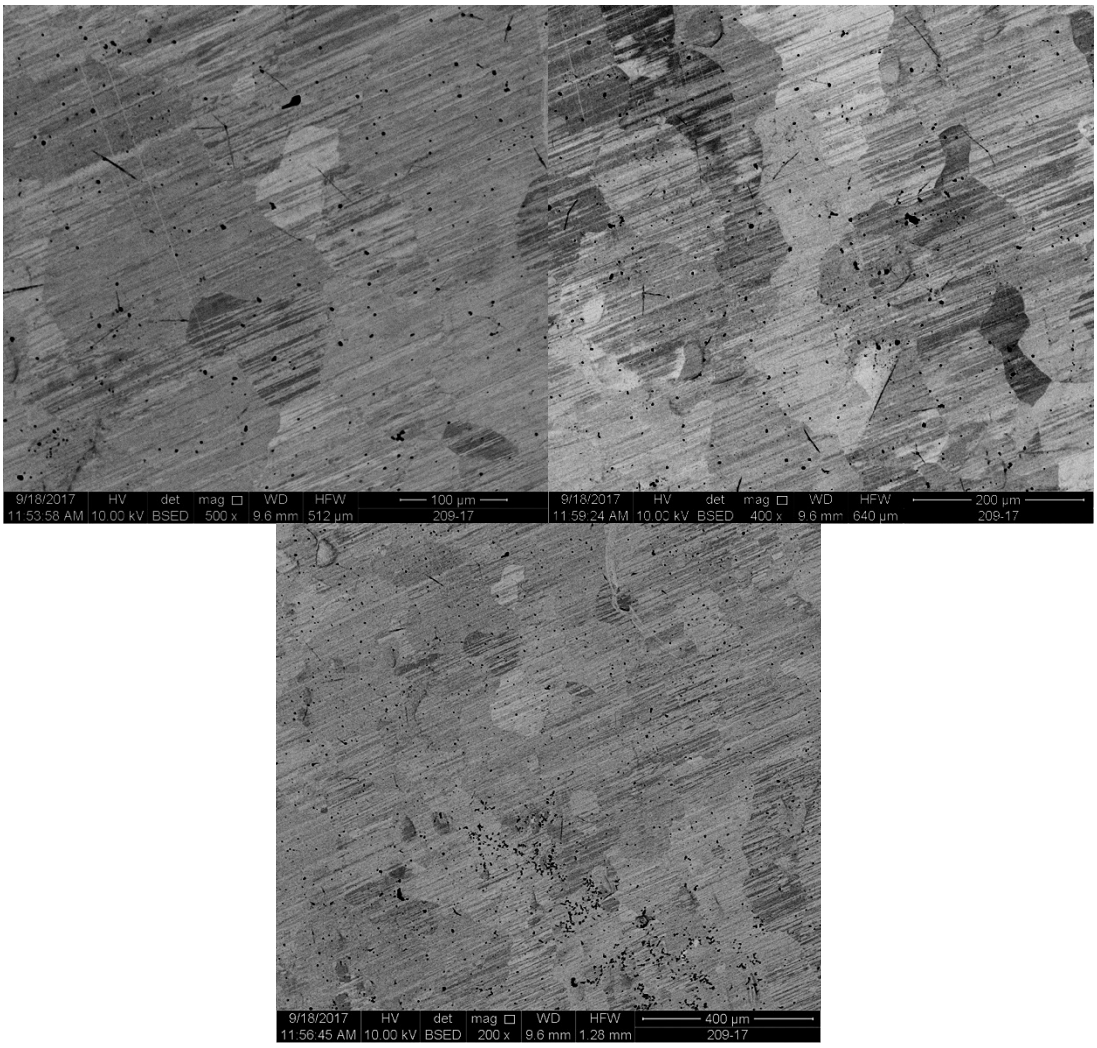

Figure 2.3 BSE images of the as-received material with high and low magnification.

For this research, each mean grain size calculation was determined by using the equivalent diameter calculation method instead of the linear intercept method due to elongated near ellipse-shaped grains. Figure 2.4 shows a schematic illustration of elongated grains.

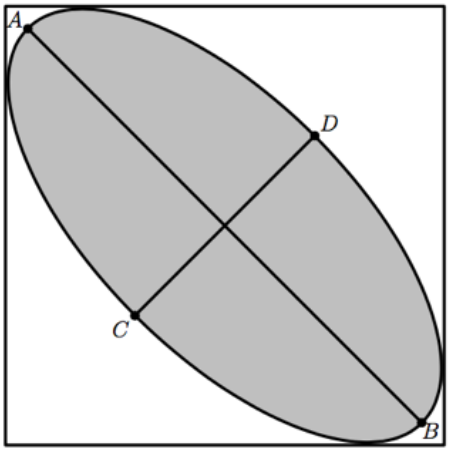

Figure 2.4 A schematic illustration of elongated near ellipse-shaped grains. |AB| and |CD| are maximum and minimum length of grains.

$$|\mathrm{AB}| = \mathrm{a} \text{ and } |\mathrm{CD}| = \mathrm{b}$$

$$d_{equivalent} = \sqrt{\frac{(a^2 + b^2)}{2}}$$

2.2 ECAE Conditions for Each Billet

The ingot was cut into 4 billets via electrical discharge machining (EDM). The billets were machined down to a 25 × 25 mm^2 cross section prior to ECAE. After EDM, we decided which ECAE parameters would be used. Table 2.2 shows the ECAE parameters of this research. As a first pass, we chose Route A for each billet. As a second pass, we chose Route C to be recovered to its near-original grain shape after Route A for each billet. After the even Cs pass, such as 2C and 4C, the microstructure shapes of the billets became

equiaxed, meaning grains have axes of almost the same length. This was important because having equiaxed grains was a sign of a successful recrystallization.

Table 2.2 The ECAE process conditions and parameters for the four billets.

	2C-900-1000°C	**2C-900-300°C**	**3C-900–700-500°C**	**2C-900-700°C**
Heat Treatment Temperature (°C) and Time	–	1200°C 2 hours	1200°C 2 hours	1200°C 2 hours
Temperature for 1st Pass(°C)	900°C	900°C	900°C	900°C
Temperature for 2nd Pass(°C)	1000°C	300°C	700°C	700°C
Temperature for 3rd Pass(°C)	–	–	500°C	–
Routes for Each Pass	1A 2C	1A 2C	1A 2C 3C	1A 2C
Extrusion Rates for Each Pass (inch/sec)	0.5 0.5	0.5 8.33×10^{-4}	0.5 0.5 0.2	0.5 0.5

Figure 2.5 shows the equal channel angular extrusion die that was used for this study. Only 3C-900-700-500 °C was exposed to three passes. Extrusions were performed at different rates. The ECAE deformation of CoCrFeMnNi was conducted at high homologous temperatures. We performed a heat treatment for all the billets at 1200 °C for two hours

to obtain homogenized material under the Argon backfill, which was used to avoid oxidation except for 2C-900-1000 °C.

Figure 2.5 Equal channel angular extrusion die to provide severe plastic deformation.

After the heat treatment and each pass, the billets were water quenched at room temperature to maintain the microstructure produced by the ECAE process and to avoid oxidation. Another method to protect material from oxidation was coating the billets with a ceramic-based glaze one-day before for every pass. Also, using a coating, such as ceramic-based glaze, was useful to conduct a smooth ECAE process and to prevent shear localization due to die chilling. Before each ECAE process, the die was preheated to 300 °C. Even though lubricant was used in the ECAE channels, during the ECAE process,

high load rate was observed. Hence, we performed only two passes for some billets, while we conducted three passes for 3C-900-700-500 °C.

2.3 EDM Process for As-ECAE-Processed Billets

After the ECAE process, the billets were cut into tension samples, compression samples, the SEM samples and the TEM samples via EDM. Figure 2.6 shows a diagram of cutting schema where FD, LD, ED stand for flow directions, longitudinal directions and extrusion directions, respectively.

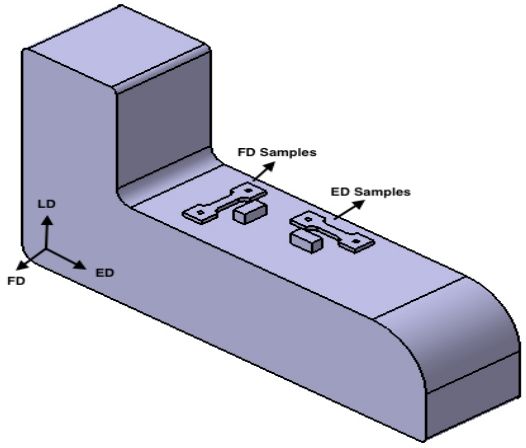

Figure 2.6 3-D billet representation during a 90º-ECAE process and the orientations of tension and compression samples on the billet.

2.4 Mechanical Tests

The mechanical properties of successfully extruded billets were reported using tension experiments and microhardness measurements in results and discussion parts. Therefore,

the preparation of the samples for each experiment and the experimental methods were briefly explained.

The preparation of the tension samples after the ECAE process was the first step. The tension samples, which were oriented parallel to the extrusion and flow direction, were cut by using EDM through longitudinal direction. Dog-bone shaped tension specimens were cut with a gage section of 8mm x 3mm with thicknesses varying from 0.45 mm to 1.30 mm whose technical drawing is shown in Figure 2.7.

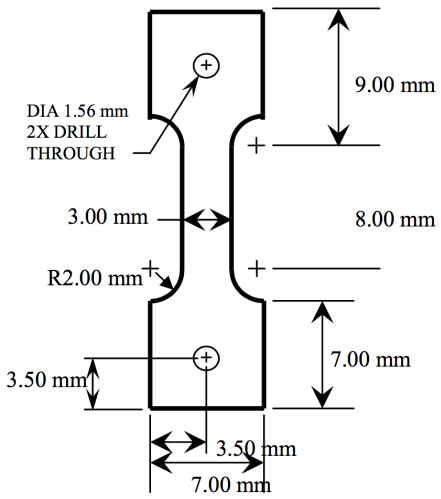

Figure 2.7 A schematic illustration of the tension samples with various thickness (0.45-1.3 mm).

Tension tests of the as-processed ECAE samples were performed using a MTS servo hydraulic test frame controlled with a Teststar II system as shown in Figure 2.8. The tension tests were done by displacement control during loading and force control during unloading. A high temperature extensometer, shown in Figure 2.9, with a gage length of

12.7 mm, was used in tension tests to record the axial strain. The tension samples were tested at a strain rate of $4x10^{-3}$ s^{-1} up to failure. Tension tests whose results were mainly classified into two groups, depending on the applied force direction: ED or FD, were performed at room temperatures. Experiments were repeated several times for each billet and for each direction to check repeatability and to minimize any errors caused by shape effects and the extensometer.

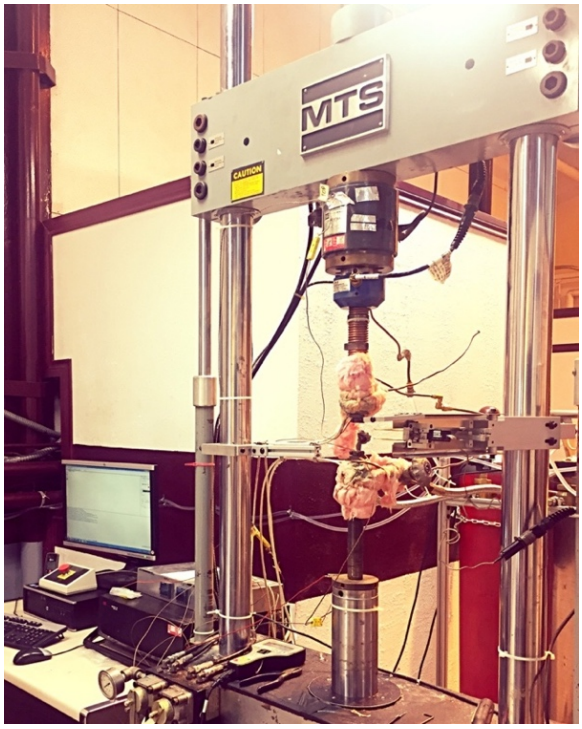

Figure 2.8 Servo hydraulic MTS load frame used for mechanical tension tests.

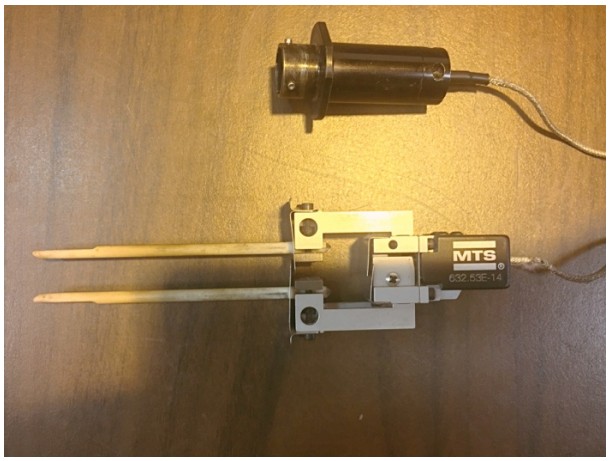

Figure 2.9 High temperature extensometer used to measure axial strain.

Additionally, as another sign of mechanical strength, hardness tests were done by using the Buehler Micromet II digital microhardness test machine. The Vickers hardness test was performed with 500 gr force. As an indenter, a square based pyramidal diamond Vickers indenter was used. Ten measurements were taken from the samples apart from each other and away from the boundary.

2.5 SEM and TEM Studies

Examining of the grain size of the EP and the FP for each billet and the as-received sample with SEM were the fundamental part of this study to find relationship between mechanical properties and microstructure. Due to the ECAE process, ultra-fine submicron grained structure was produced. Therefore, with usual preparation, the observation of submicron grains was hard with SEM. In this section, the preparation of the EP and the FP samples from each billet, and the as-received samples were explained. We followed the steps of sectioning, mounting, polishing and electropolishing, or using the Vibromet machine to

examine them at optical microscope and SEM. Sectioning was the first step which minimized the areas of the samples by using the Buehler Isomet 1000 diamond saw with a water based lubricant. After the first step, the sectioned samples were mounted with a mixture of epoxy and epoxy hardener. Then, polishing was performed starting from 400 to 1200 grit SiC paper. After SiC paper, special suspensions were used such as 6, 3, 1 and 0.25 µm diamond suspensions, 0.5 µm Al_2O_3 powder, and colloidal silica having a particle size of 60 nm. Lastly, electropolishing or vibratory polisher was used. Since there was a lack of information in the ECAE process of CoCrFeMnNi HEA, numerous techniques were tried to see nanosized grains at the SEM studies. One of the successful methods was electropolishing. Figure 2.10 shows the setup for electropolishing. The samples were electropolished with 16 volume % H_2SO_4 in a methanol solution at 0 ºC to protect from over etching. First, to figure out optimum voltage for CoCrFeMnNi HEA, dummy samples were used and the voltage of power supply was gradually increased. The data from the computer was then collected and a graph was drawn, shown in Figure 2.11.

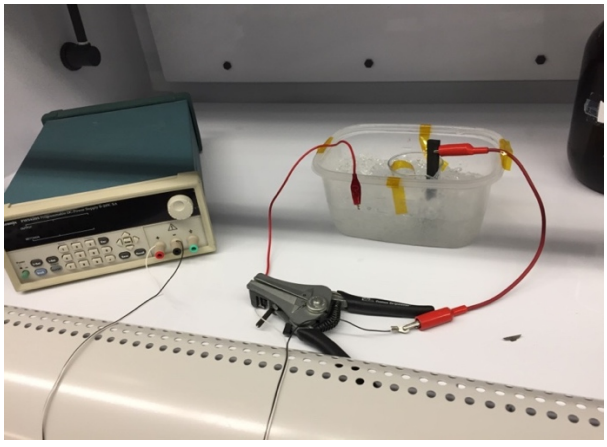

Figure 2.10 Electropolishing setup utilized throughout the research.

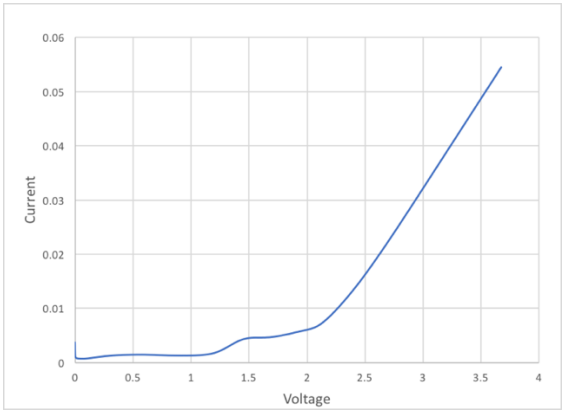

Figure 2.11 Current and voltage relationship of equimolar CoCrFeMnNi HEA during electropolishing.

As seen from Figure 2.11, the optimum voltage for equimolar CoCrFeMnNi HEA ranges between 1.5 and 2 voltages, which could vary with the different this power supply and the different setup conditions. As a final step, the electropolishing of each sample was completed between 30 to 60 seconds depending on surface quality and sample thickness. Another option as a final step was the VibroMet 2 vibratory polisher machine as shown in Figure 2.12. Before decided to use the VibroMet 2 vibratory polisher as a final step, the samples were polished starting from 400 to 600 grit SiC and then 0.5 µm Al_2O_3 powder. Then, the samples were polished for a few days with non-dry colloidal silica having a particle size of 60 nm.

Figure 2.12 VibroMet 2 vibratory polisher to prepare high quality polished surfaces.

The SEM study was performed for secondary electron (SE) imaging and backscattered secondary electron (BSE) imaging of the as-received and the as- processed ECAE samples for the EP and the FP of each billet. For the SEM studies, FEI Quanta 600 FE-SEM was used with high magnification and low accelerating voltage as shown in Figure 2.13.

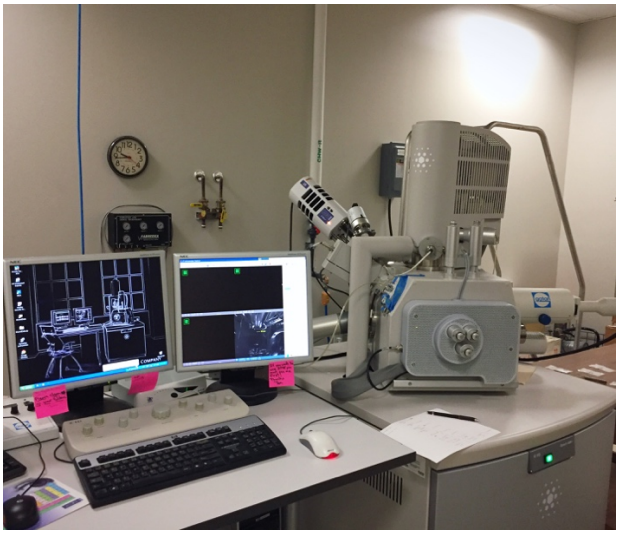

Figure 2.13 FEI Quanta 600 FE-SEM used for high-resolution imaging of surfaces.

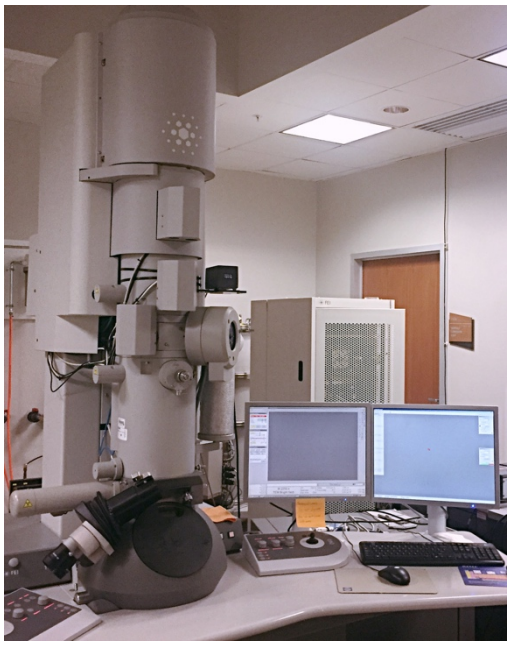

Figure 2.14 FEI Tecnai G2 F20 –TEM used for providing high-magnification images of the internal structure of samples.

Samples for the TEM examination were prepared by grinding, mechanical polishing of slice down to 0.1 mm, punching 3mm foils. The TEM study was performed on the as-processed 2C-900-300 °C FP and 3C-900-700-500 °C FP. Prepared 2C-900-300 °C FP and 3C-900-700-500 °C FP foils were twin jet electropolished with 20 volume % H_2SO_4 in a methanol solution at -20 ºC.

The TEM study was conducted with FEI Tecnai G2 F20 –TEM at 200 kV for thin foils of 2C-900-300 °C FP and 3C-900-700-500 °C FP. Figure 2.14 shows the TEM which was used for this study. Figure 2.15 shows the summary of the experimental process.

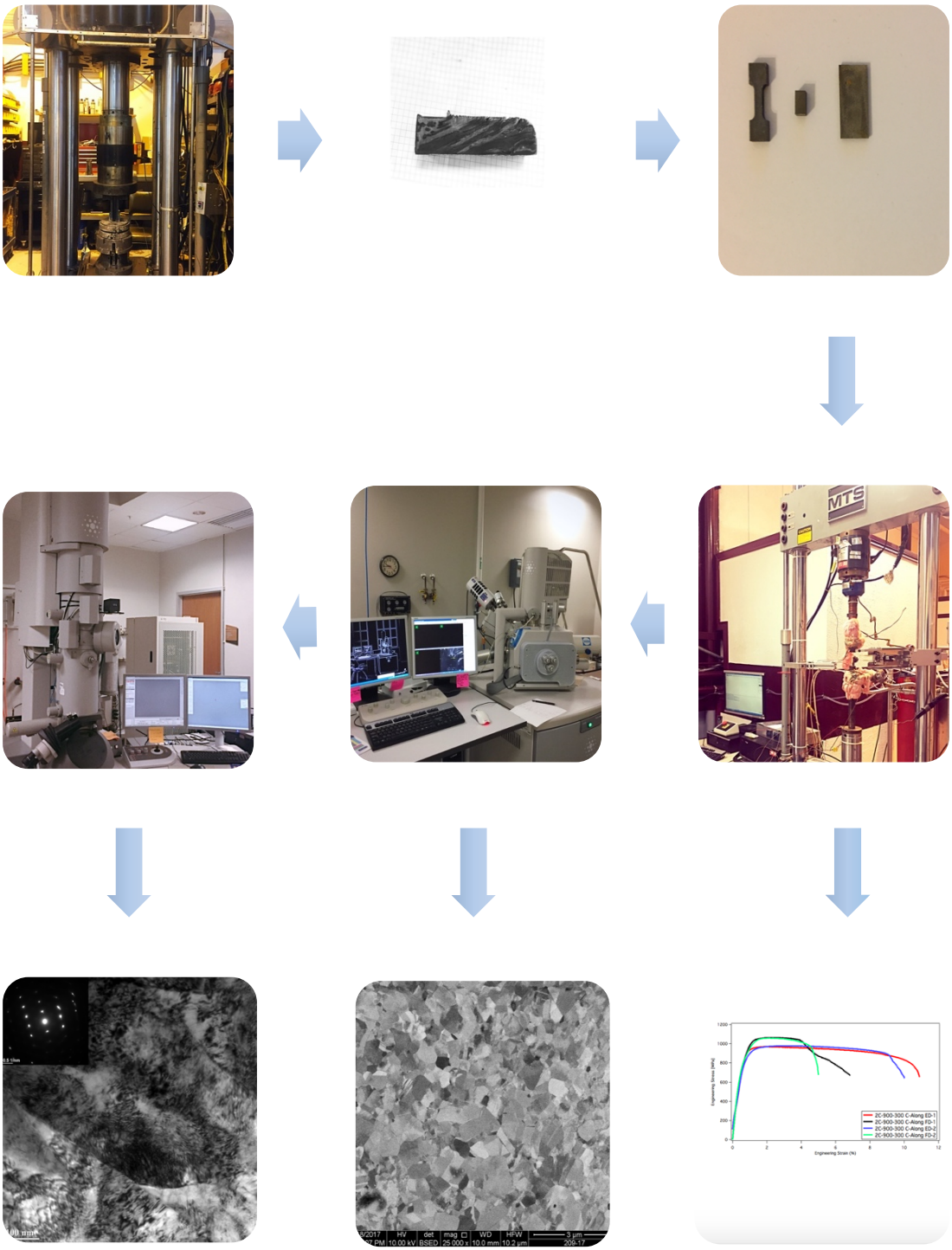

Figure 2.15 Summary of experimental methods utilized throughout the research.

CHAPTER III

RESULTS AND DISCUSSIONS ON 2C-900-1000 °C

3.1 ECEA Conditions and Processing of 2C-900-1000 °C

The as-received equiatomic CoCrFeMnNi HEA initially heated up to 900 °C for 30 minutes. Meanwhile, the ECAE die was preheated to 300 °C. The as-received CoCrFeMnNi billet was extruded in a 90° die. For the first pass, the extrusion took place at a rate of 0.5 inch/sec. After the first pass, the billet was water quenched to protect the microstructure that was successfully achieved during the ECAE process. After each pass, the billets were water quenched. During the first pass, we achieved a very high load; therefore, we increased the temperature of the second pass to 1000 °C. For the second pass, the billet was reheated to 1000 °C for 30 minutes and with the same extrusion rate; the second pass was completed successfully. Figure 3.1 summarizes all the conditions for 2C-900-1000 °C.

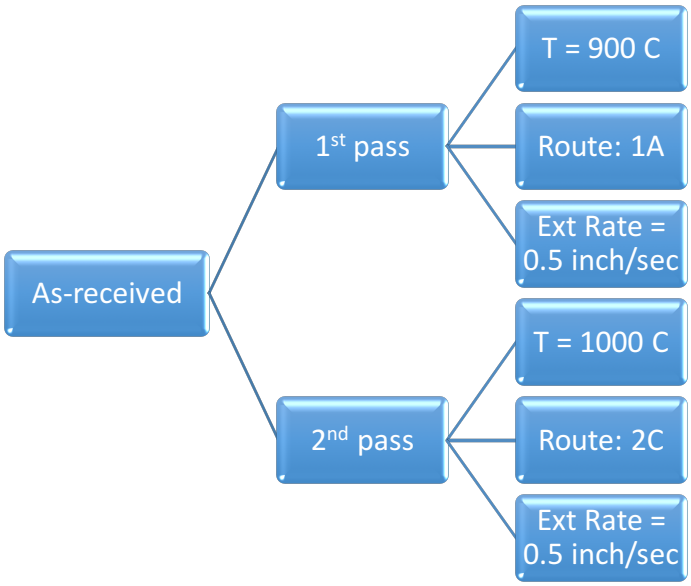

Figure 3.1 The flowchart of the ECAE processed 2C-900-1000 °C material.

3.2 Microstructure Evaluation After ECAE

After the ECAE process, we examined the FP and the EP of 2C-900-1000 °C with SEM to evaluate the grain size of the samples. Figure 3.2 shows the BSE images of 2C-900-1000 °C on the extrusion plane with high and low magnification. It can be seen that the microstructure consisted of both equiaxed and somewhat elongated grains. The long axes of the elongated grains were near parallel to the shear direction. The mean grain size of 2C-900-1000 °C on the extrusion plane was 0.48 ± 0.16 μm, which was calculated by the equivalent diameter method, whereas there were also some other grains whose sizes are up to 1.5 ± 0.5μm containing poorly defined dislocation arrangements.

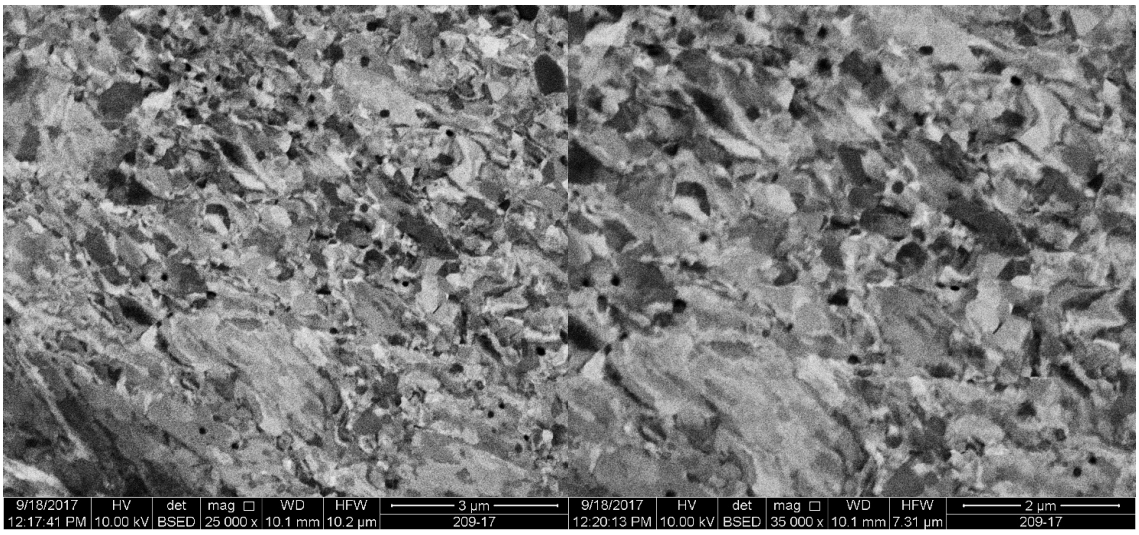

Figure 3.2 BSE images of the as-processed 2C-900-1000 °C ECAE material on the EP with low and high magnification.

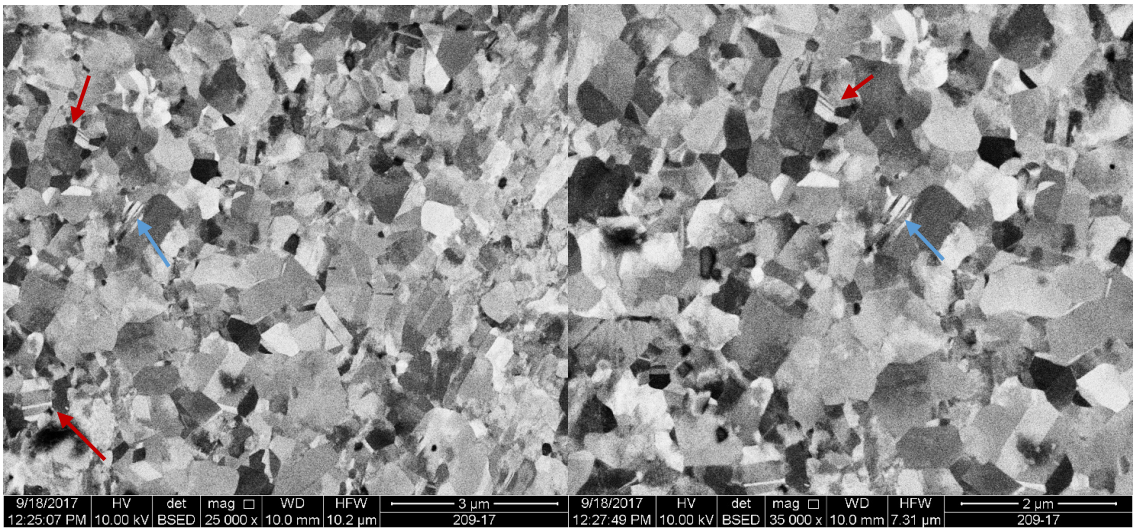

Figure 3.3 BSE images of the as-processed 2C-900-1000 °C ECAE material on the FP with low and high magnification.

Figure 3.3 shows the SEM images of 2C-900-1000 °C on the flow plane with high and low magnification. The microstructure of 2C-900-1000 °C on the flow plane was most

likely to be equiaxed. The mean grain size of 2C-900-1000 °C on the flow plane was 0.67 ± 0.18μm. In Figure 3.3, we observed annealing and deformation twinning mechanisms, which were shown with red and blue arrows, respectively. Even at a high temperature, we achieved small equiaxed grains and occasionally deformation twinning. It could be because of high strain rate during the ECAE process.

3.3 Mechanical Behavior After ECAE

In [25], Otto showed tensile test results of the as-received samples with a mean grain size 155μm at room temperature. He stated that yielding stress and ultimate tensile stress of as-cast material were around 165 and 500 MPa, respectively. For our as-cast material, we expected the same results for yielding stress because of very similar grain size effect. After 2C-900-1000 °C ECAE, on the extrusion plane, the increase in yielding stress was almost 5 times larger than the as-received material with more than 20% strain. On the other hand, with the same ECAE-processed sample along flow directions, the results were a bit different than the extrusion direction. The yielding stress of the samples was still almost 4 times greater than the as-received one, yet 2C-900-1000 °C-FD was not as ductile as 2C-900-1000 °C-ED as shown in Figure 3.4. Some mechanical properties, such as ductility, depend on the orientation of the grains and the texture of the billets. As further research, the texture and grain orientation can be investigated in detail to understand the reason behind the different strains.

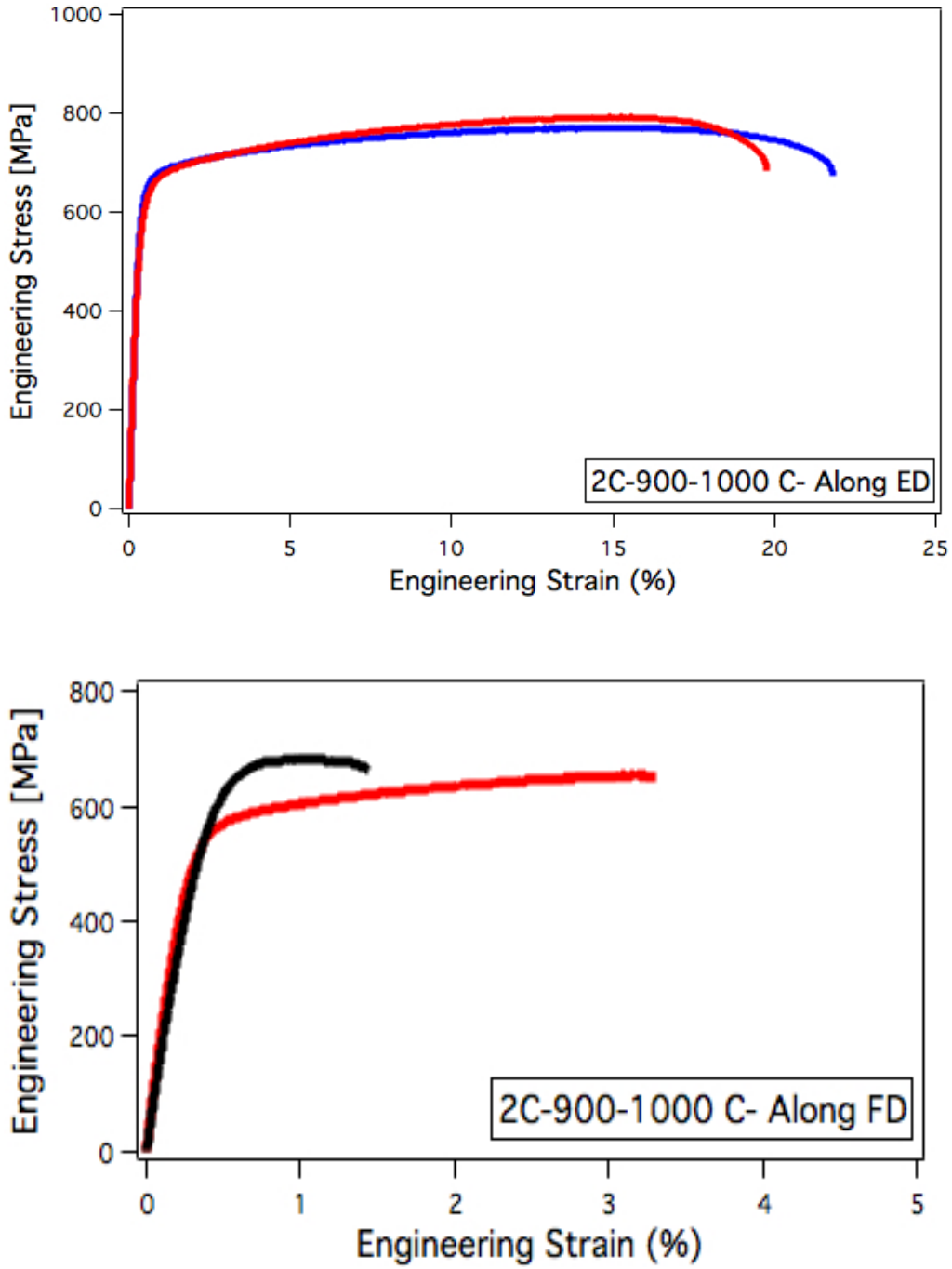

Figure 3.4 The tensile engineering stress-strain curves of the ECAE processed 2C-900-1000 °C samples along the ED and the FD, respectively.

As another sign of strength of the material, the Vickers hardness test was conducted for as-received material and the first and the second pass of 2C-900-1000 °C materials. The hardness of the as-cast materials was around 140 HV, while the hardness of the first pass sample was almost 2 times greater than that of the as-received material. Hardness results of the first and the second pass of 2C-900-1000 °C were almost the same.

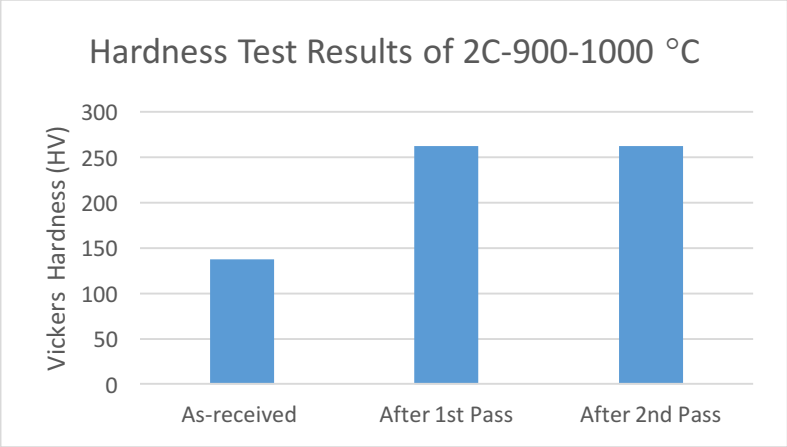

Figure 3.5 The hardness test results of as-received material and the ECAE processed 2C-900-1000 °C samples after the first pass and after the second pass.

We thought that after the ECAE process, the porosity coming from as-cast material could be closed down, yet as can be seen from Figure 3.6, we could not close them down. In fact, the reason why we could not achieve more ductility for this billet could be expressed with these porosity clusters. They were smaller than as-cast porosities, but they were more homogenized among the billet. Therefore, initial porosity affected the void nucleation and the crack propagation significantly. We could achieve more ductile materials after ECAE if we would get rid of as-cast porosity.

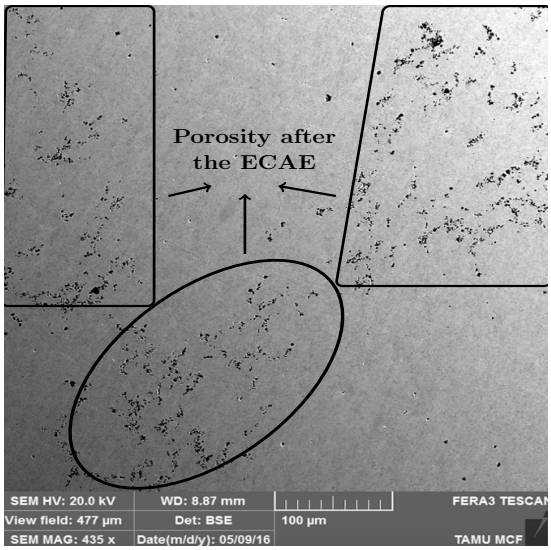

Figure 3.6 Porosity clusters inside as-ECAE-processed 2C-900-1000 °C material.

CHAPTER IV

RESULTS AND DISCUSSIONS ON 2C-900-300 °C

4.1 ECEA Conditions and Processing of 2C-900-300 °C

Heat treatment was conducted for the as-received equiatomic CoCrFeMnNi HEA with the Argon backfill for 2 hours at 1200 °C to homogenize the sample before the ECAE process. Then, the billet was water quenched at room temperature. Afterwards, it was heated up to 900 °C for 30 minutes. Meanwhile, the ECAE die was preheated to 300 °C. The as-received CoCrFeMnNi billet was extruded. For the first pass, the extrusion took place at a rate of 0.5 inch/sec. After the first pass, the billet was water quenched to protect the microstructure that was successfully achieved during the ECAE process, as mentioned in Section 3.2. For the second pass, the billet was reheated to 300 °C for 30 minutes, and the second pass was completed successfully with the very low extrusion rate (8.33×10^{-4}). We chose slow extrusion rate at 300 °C because it is hard to perform ECAE at room temperature. Therefore, when the temperature decreases, to protect the billet and the ECAE die, we should proceed the ECAE process at a low extrusion rate. Figure 4.1 summarizes all the conditions for 2C-900-300 °C.

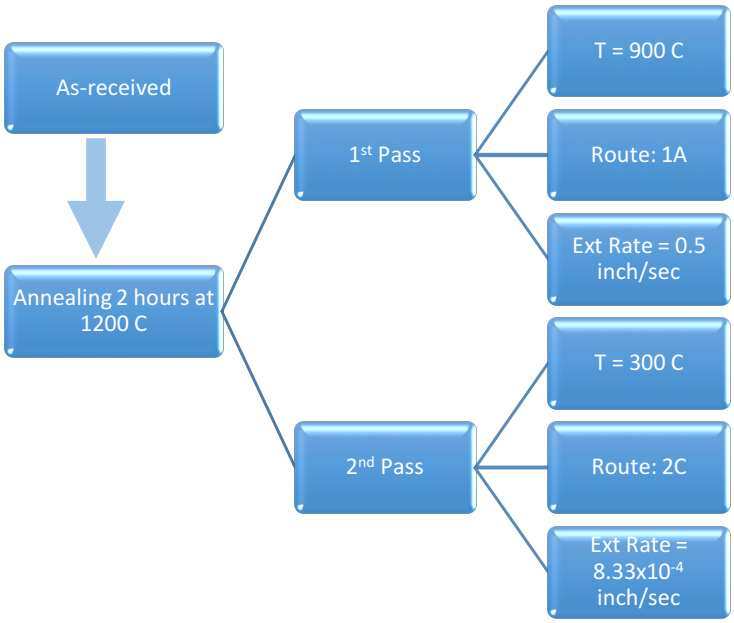

Figure 4.1 The flowchart of the ECAE processed 2C-900-300 °C material.

4.2 Microstructural Evaluation After ECAE

Figure 4.2 shows the SEM images of 2C-900-300 °C on the extrusion plane with low magnification quality. As can be seen in Figure 4.2, the microstructure consisted of both large equiaxed and somewhat small elongated grains. The mean grain size of 2C-900-300 °C on the extrusion plane was 0.63 ± 0.1 μm, which was calculated by the equivalent diameter method. However, there were also some other grains whose sizes were up to 1 ± 0.3 μm. The reason why some grains' sizes were remarkably larger than the rest is containing poorly defined dislocation arrangements.

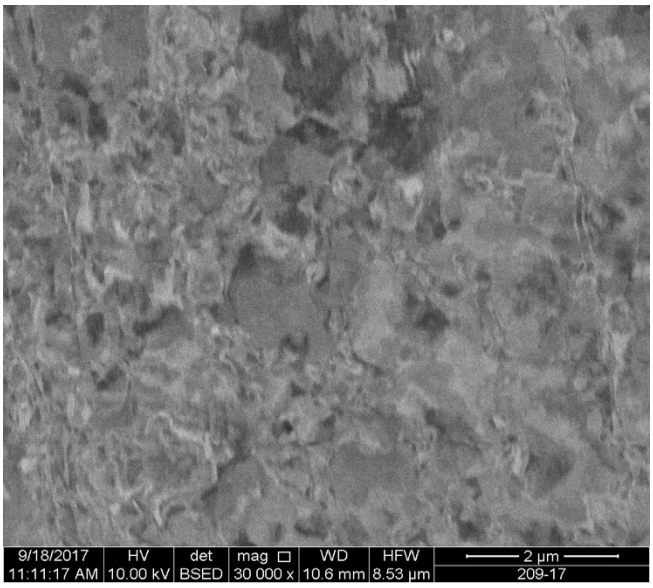

Figure 4.2 BSE images of the as-processed 2C-900-300 °C ECAE material on the EP with low magnification.

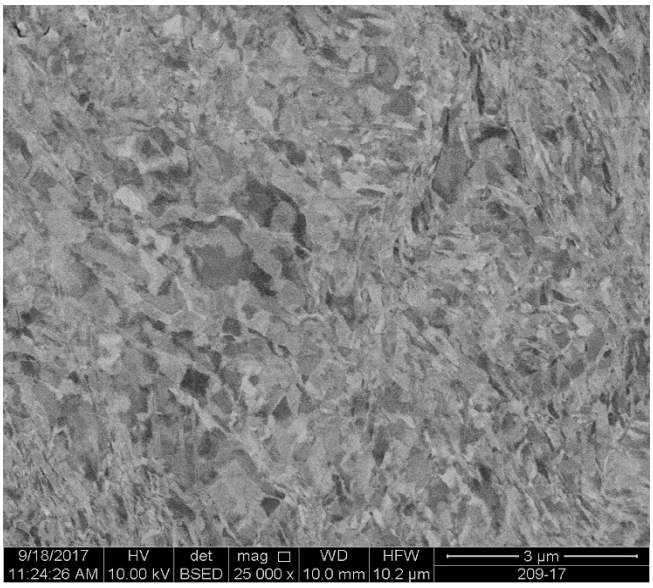

Figure 4.3 BSE images of the as-processed 2C-900-300 °C ECAE material on the FP with low magnification.

Figure 4.3 shows the SEM images of 2C-900-300 °C on the flow plane with low magnification. The investigation of the microstructure with high magnification was performed. The microstructure consisted of elongated grains. The mean grain size of 2C-900-300 °C on the flow plane was 0.43±0.09 μm, which was calculated by the equivalent diameter method. On the other hand, there were also some other grains whose sizes were up to 0.67±0.1 μm.

The TEM study was conducted on the flow plane of the as-processed 2C-900-300 °C ECAE sample. The reason why the TEM sample was conducted for this sample is to observe annealing and deformation twinning. We did not investigate any twinning for this sample via the SEM. Therefore, we wanted to make sure whether or not there was a twinning mechanism for this samples.

Figure 4.4 shows the bright field TEM micrographs of 2C-900-300 °C on the FP. These were the proofs that the quite refined structure was achieved by the ECAE process. Figure 4.5 indicates that the most significant finding with the TEM studies was deformation twinning. This was the first-time that deformation twinning were detected at such high homologous temperatures because of a high rate deformation, which was caused by the ECAE process.

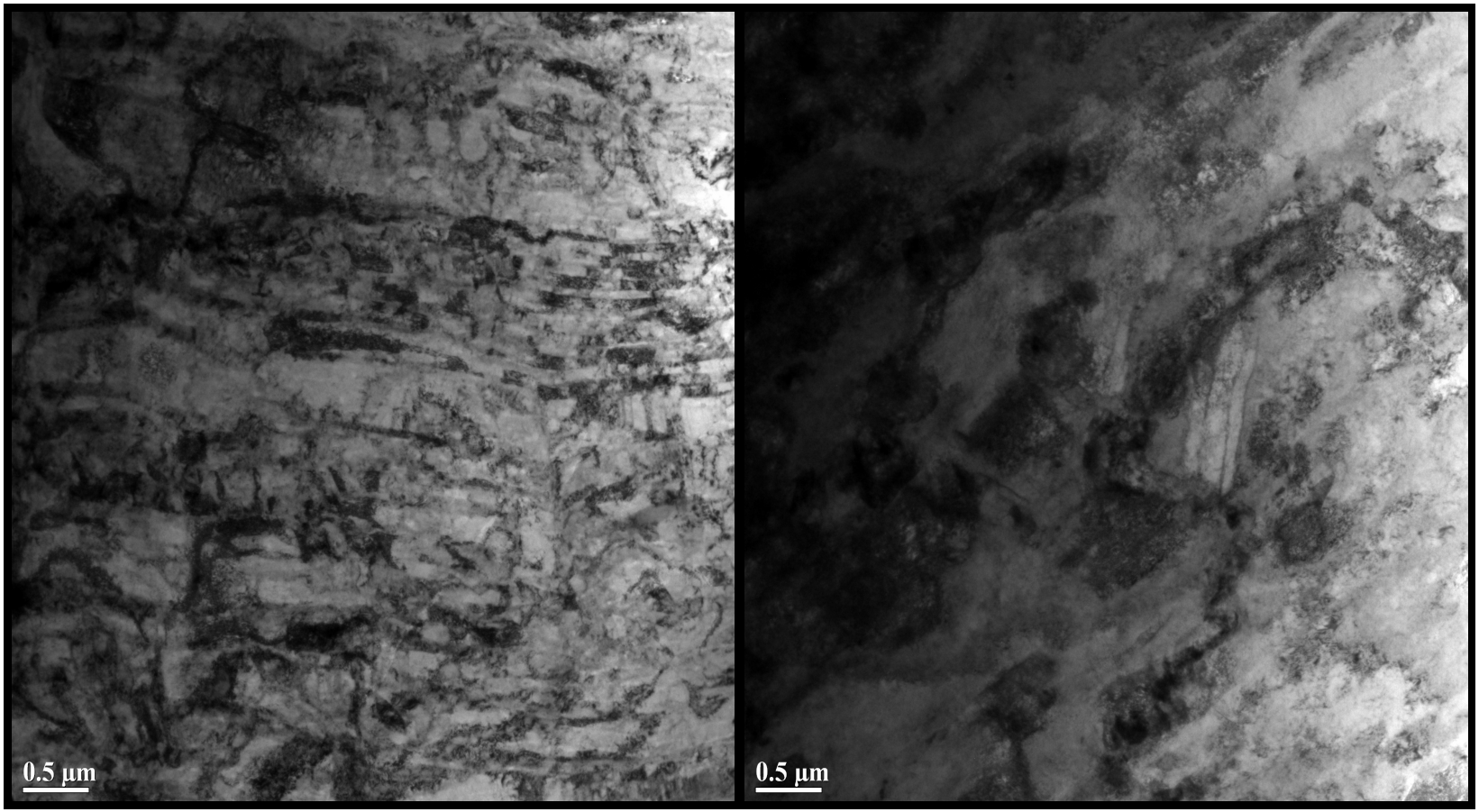

Figure 4.4 Bright-field TEM images of 2C-900-300 °C processed material on the FP.

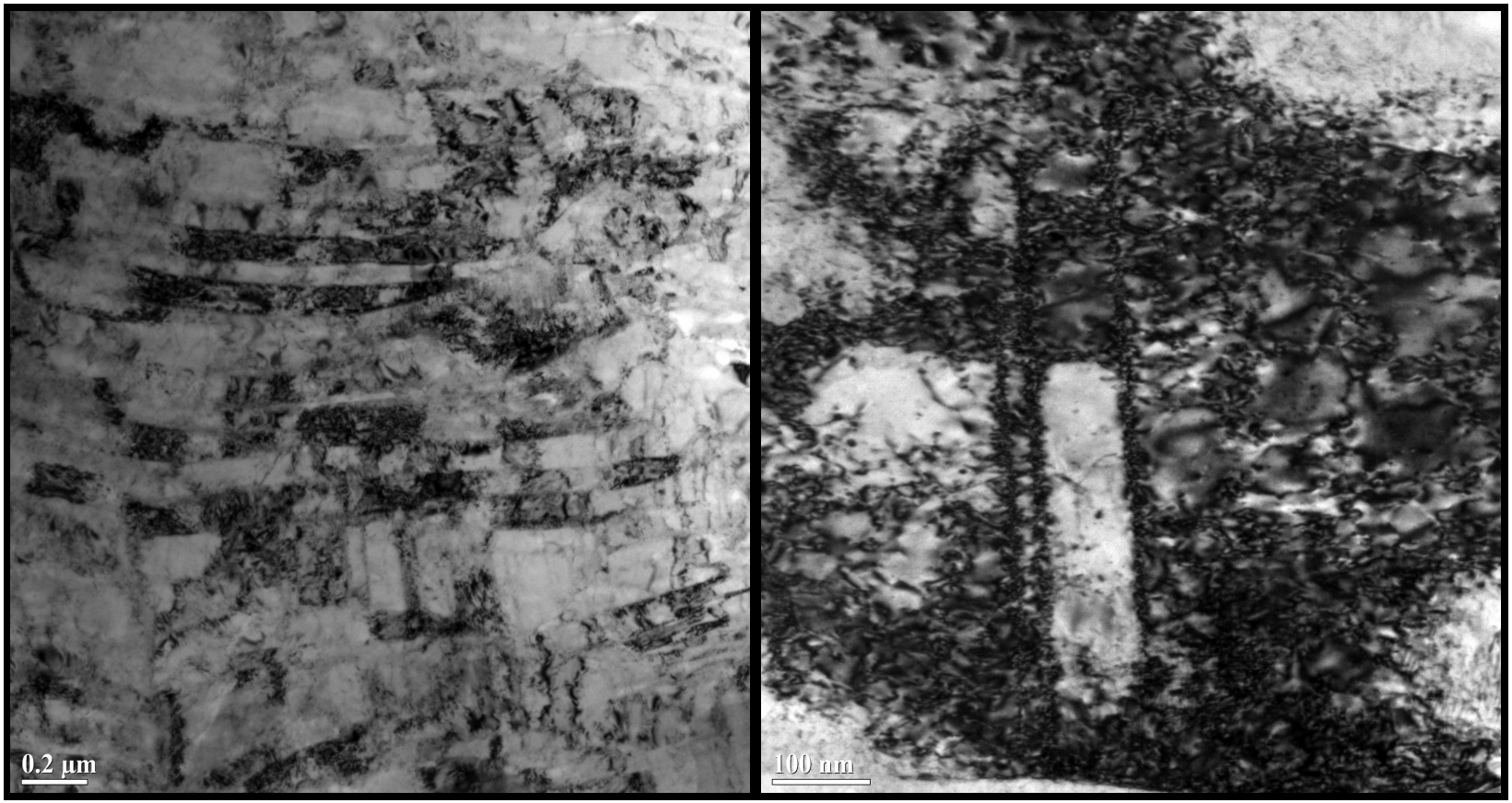

Figure 4.4 Continued.

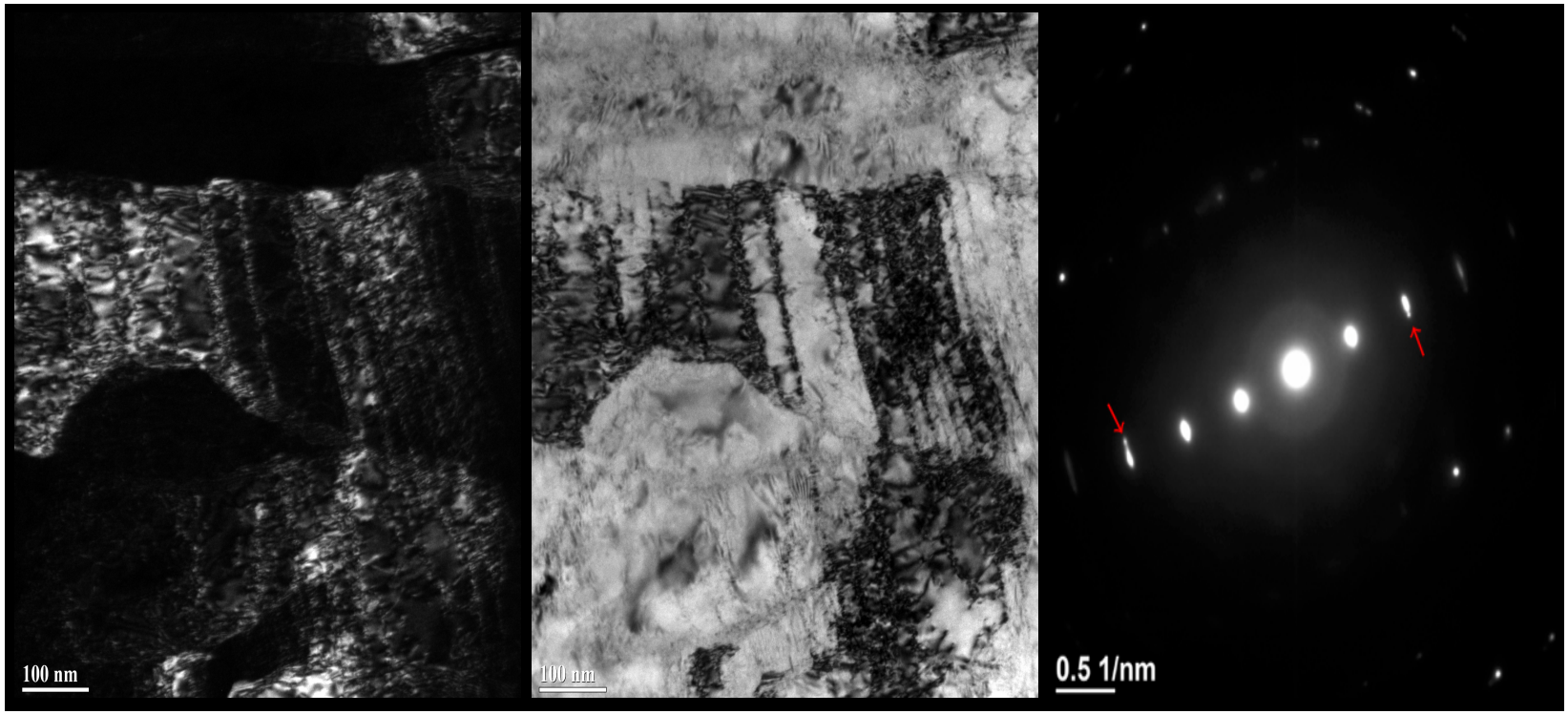

Figure 4.5 Dark-field, bright-field and diffraction pattern TEM images of 2C-900-300 °C processed material on the FP.

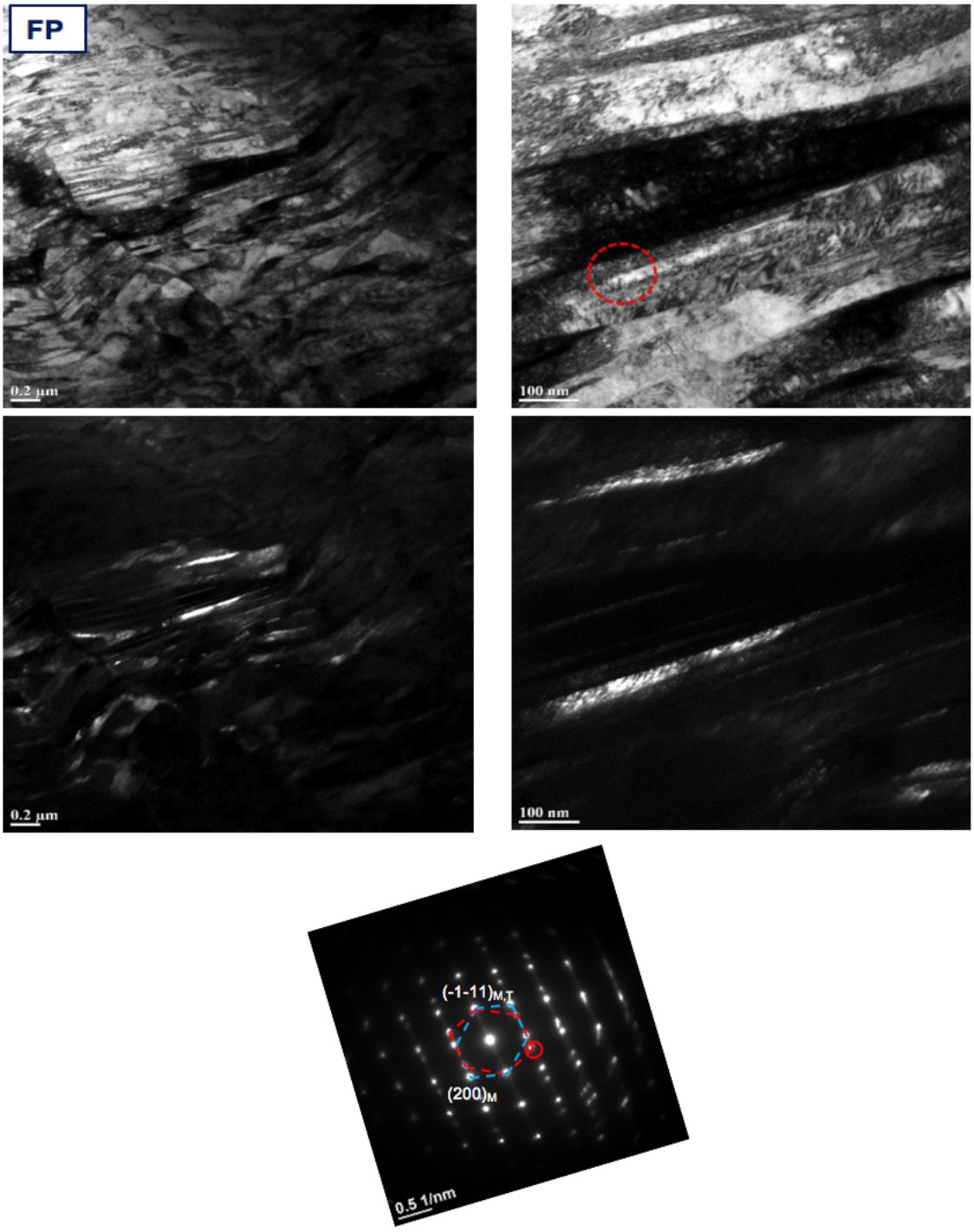

Figure 4.5 Continued.

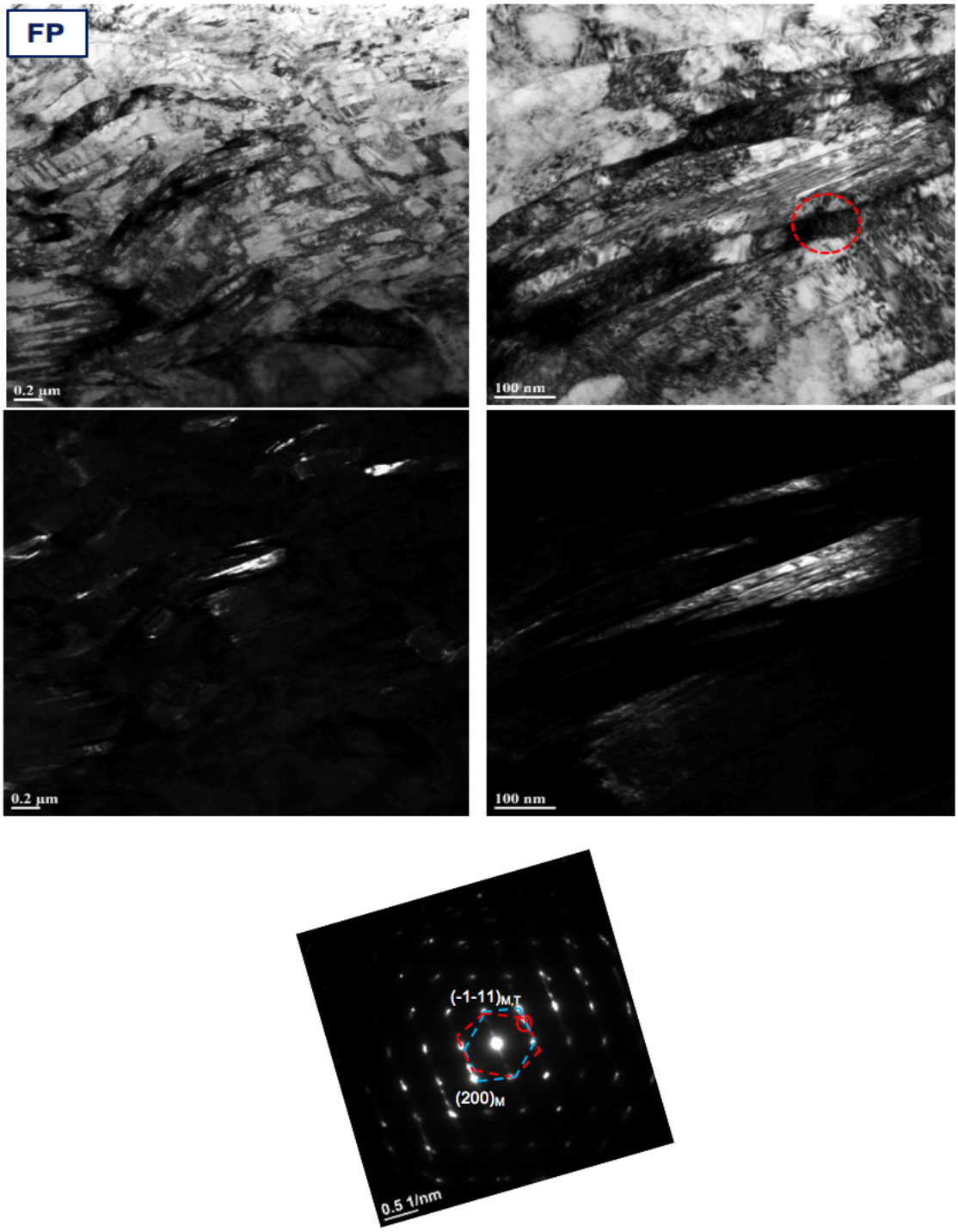

Figure 4.5 Continued.

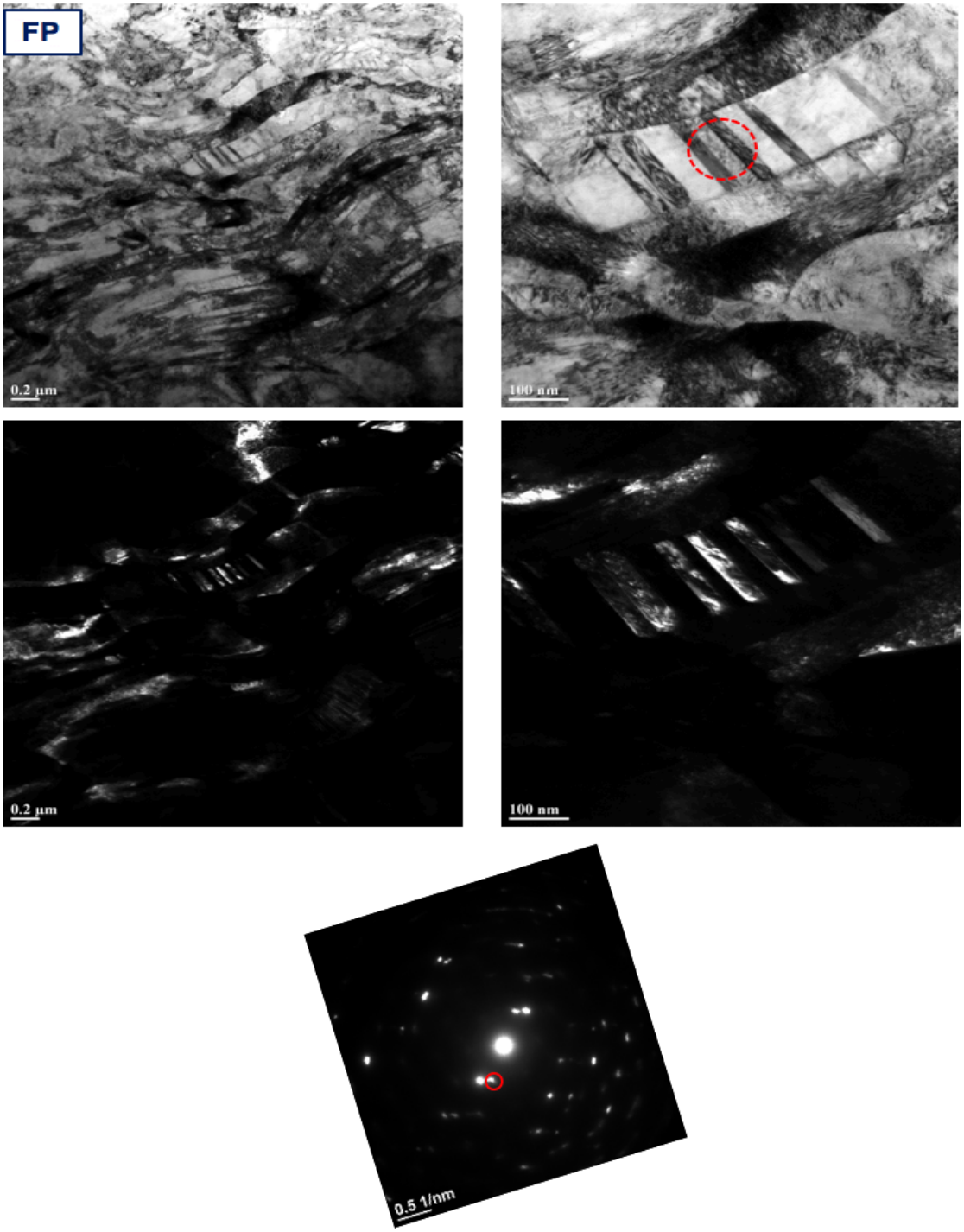

Figure 4.5 Continued.

4.3 Mechanical Behavior After ECAE

As we know, there is a trade-off between strength and ductility of the ECAE materials. When strength increases, the material usually shows brittle mechanical properties. Compared with 2C-900-1000 °C, there was an increase in the yielding stresses of the 2C-900-300 °C samples, whereas there was a drop in ductility as shown in Figure 4.6. The yielding stress of the 2C-900-300 °C ECAE sample along the ED was almost 6 times greater than the as-received one and 1.4 times greater than the 2C-900-1000 °C ECAE sample along the ED. On the other hand, 2C-900-300 °C-ED was not as ductile as 2C-900-1000 °C-ED. The engineering strain of 2C-900-300 °C-ED was around 12%. Similar to 2C-900-1000 °C, there was an increase in the yielding stress of 2C-900-300 °C-FD and a decrease in ductility compared with 2C-900-300 °C-ED. Some mechanical properties, such as ductility, depend on the orientation of the grains and the texture of the billets. As further research, the texture and grain orientation can be investigated in detail to understand the reason behind the different strain rates.

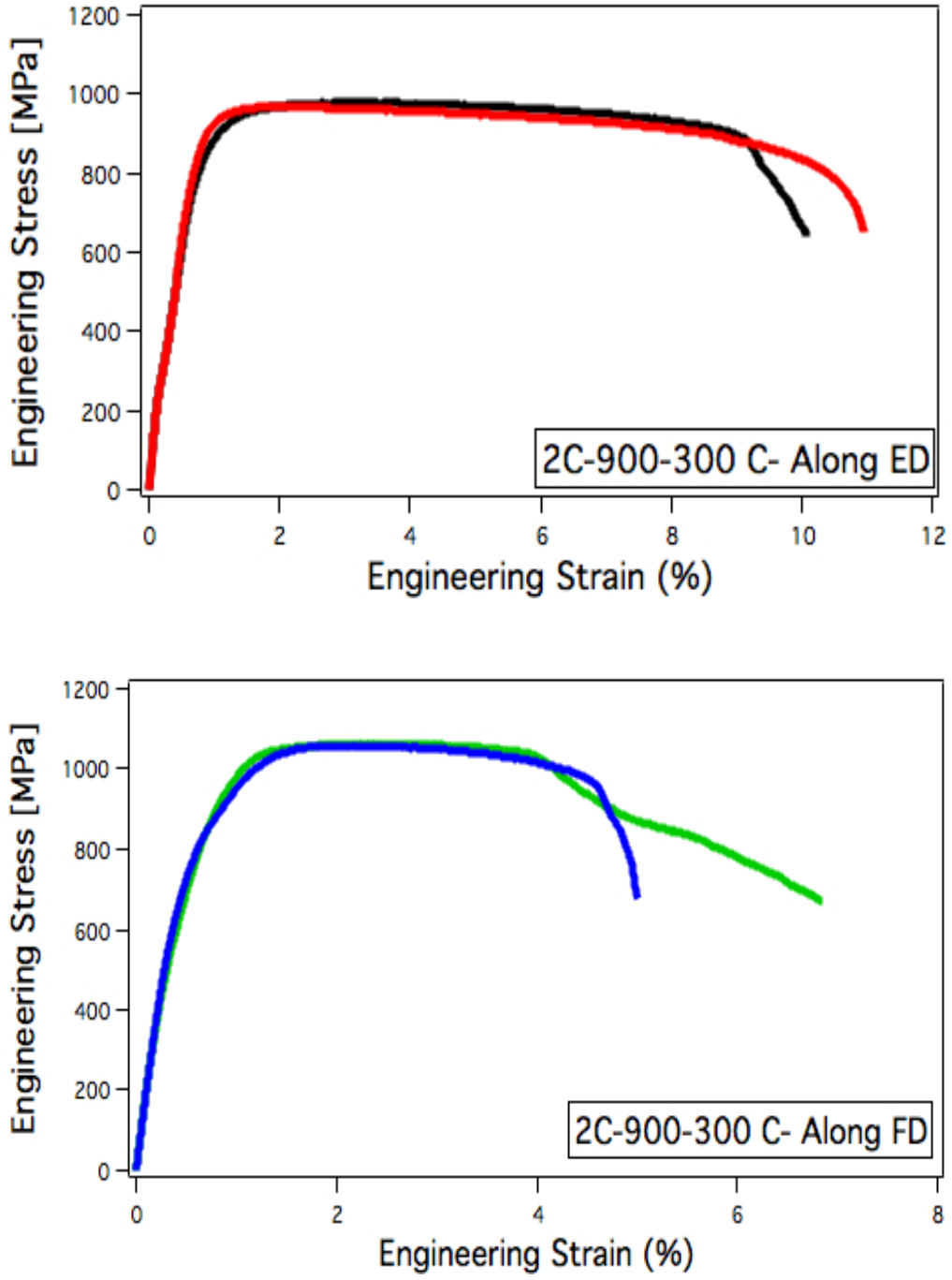

Figure 4.6 The tensile engineering stress-strain curves of the ECAE processed 2C-900-300 °C samples along the ED and the FD, respectively.

In addition to traditional tensile tests, a tension test with DIC method was performed for this billet along the ED. Figure 4.7 shows the stress field during the experiment. With the set of the images, the stress field was analyzed on the sample. For example, the red color region was the high stress field which means propagation of the crack was on that field.

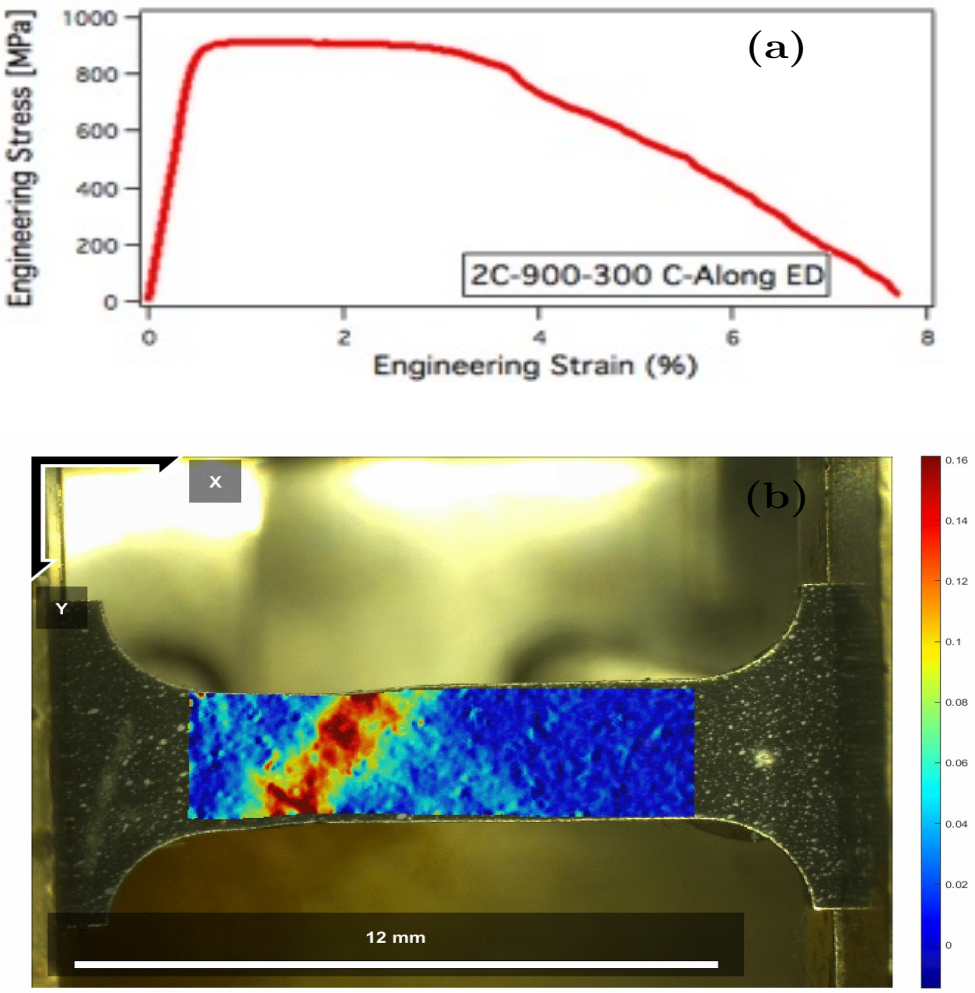

Figure 4.7 (a) The tensile engineering stress-strain curve along the ED, and (b) one of the DIC images during the experiment with the stress field.

CHAPTER V

RESULTS AND DISCUSSIONS ON 3C-900-700-500 °C

5.1 ECEA Conditions and Processing of 3C-900-700-500 °C

Similar to the 2C-900-300 °C billet, heat treatment was conducted for the as-received equiatomic CoCrFeMnNi HEA with the Argon backfill for 2 hours at 1200 °C to homogenize the sample before the ECAE process. Then, the billet was water quenched at room temperature. Afterwards, it was heated up to 900 °C for 30 minutes. Meanwhile, the ECAE die was preheated to 300 °C. The as-received CoCrFeMnNi billet was extruded at a rate of 0.5 inch/sec following Route A. After the first pass, the billet was water quenched to protect the microstructure that was successfully achieved during the ECAE process.For the second pass, the billet was reheated to 700 °C for 30 minutes and the second pass was completed successfully following Route C with the same extrusion rate. For the third pass, Route C was followed with slower extrusion rate (0.1 inch/sec) than the previous ones. Figure 5.1 summarizes all the conditions for 3C-900-700-500 °C.

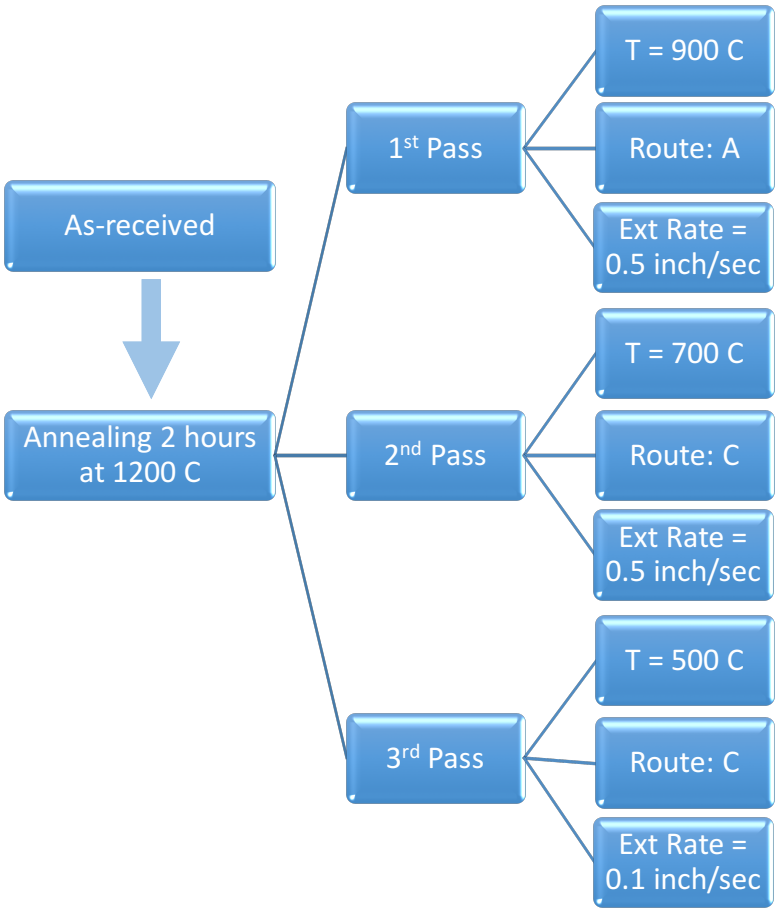

Figure 5.1 The flowchart of the ECAE processed 3C-900-700-500 °C material.

5.2 Microstructural Evaluation After ECAE

Figure 5.2 shows the SEM images of 3C-900-700-500 °C on the extrusion plane with low magnification. The microstructure consisted very small grains. The mean grain size of 3C-700-500-300 °C on the extrusion plane is 0.29 ±0.07 μm, which is almost 690 times smaller than the as-received grains.

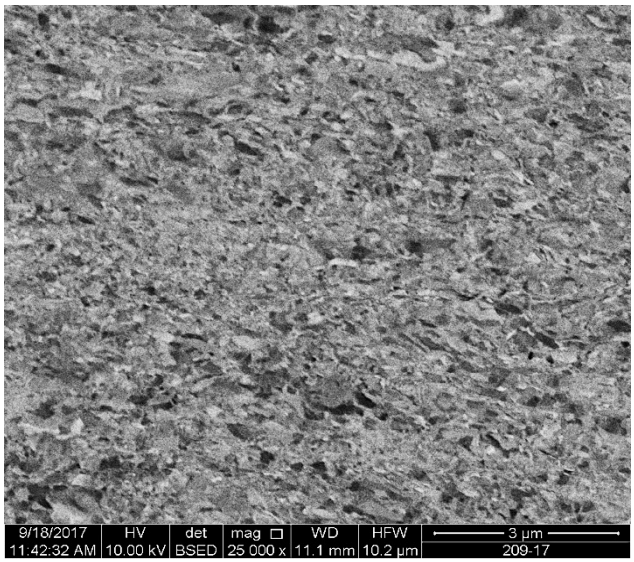

Figure 5.2 BSE images of the as-processed 3C-900-700-500 °C ECAE material on the EP with low magnification.

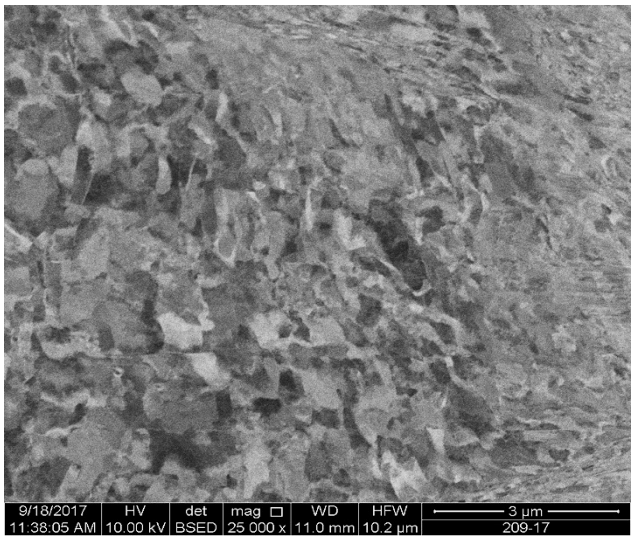

Figure 5.3 BSE images of the as-processed 3C-900-700-500 °C ECAE material on the FP with low magnification.

Figure 5.3 shows the SEM images of 3C-900-700-500 °C on the flow plane with low magnification. The microstructure consisted of both equiaxed and somewhat elongated

grains. The mean grain size of 3C-900-700-500 °C on the flow plane was 0.57 ±0.15 μm, which was almost twice greater than that of 3C-900-700-500 °C on the extrusion plane.

The TEM study was conducted on the flow plane of the as-processed 2C-900-300 °C ECAE sample. The reason why the TEM sample was conducted for this sample is to observe annealing and deformation twinning. We did not investigate any twinning for this sample via SEM. Therefore, we wanted to make sure whether or not there was a twinning mechanism for this samples.

Figure 5.4 shows the bright field TEM micrographs of 3C-900-700-500 °C on the FP. They were the proofs that quite refined structure was achieved by the ECAE process. Figure 5.5 indicates that the most significant finding with the TEM studies wass deformation twinning. This was the first-time that deformation twinning was detected at such high homologous temperatures because of a high rate deformation caused by the ECAE process.

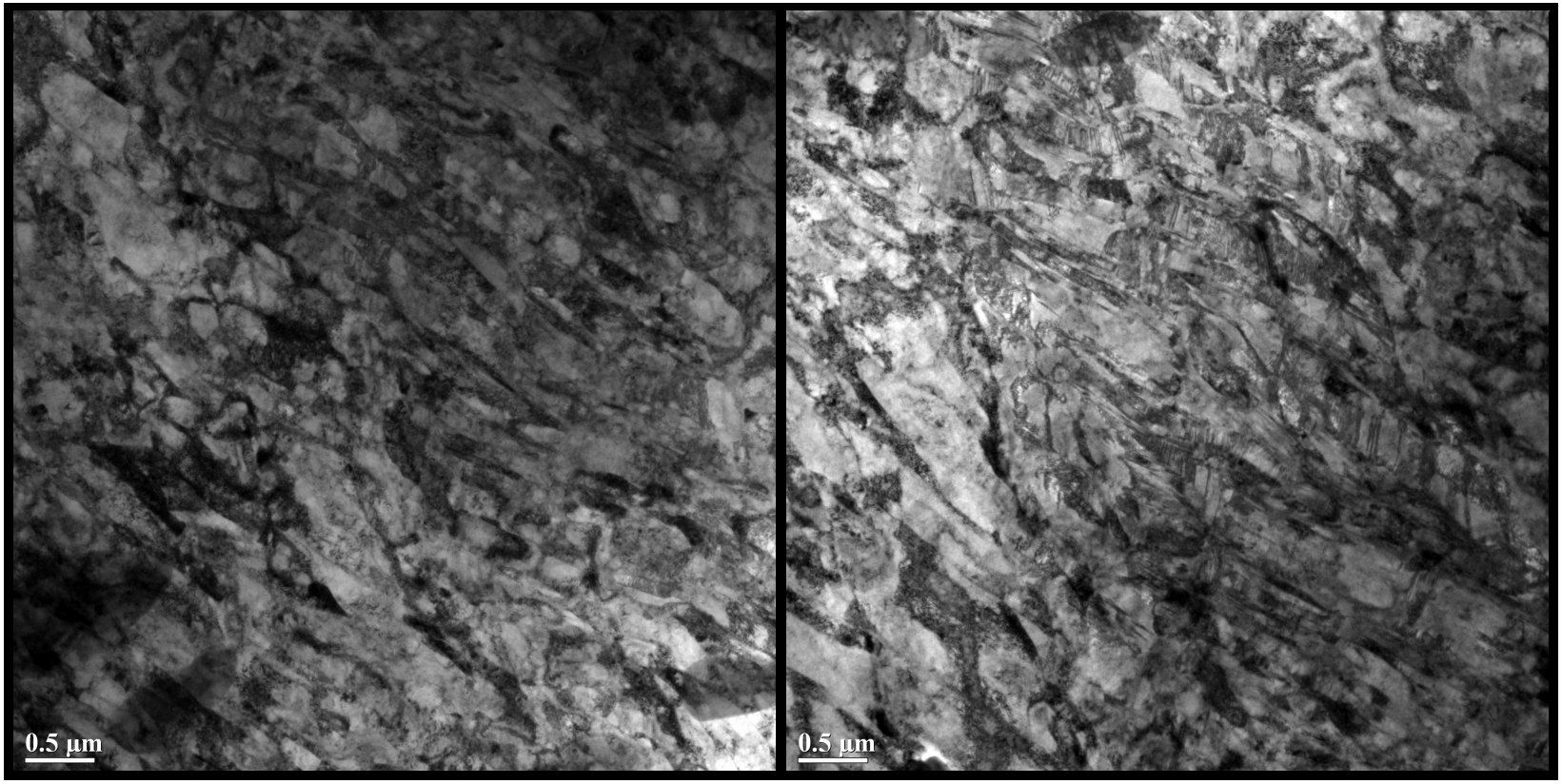

Figure 5.4 TEM images of the as-processed 3C-900-700-500 °C ECAE material on the FP.

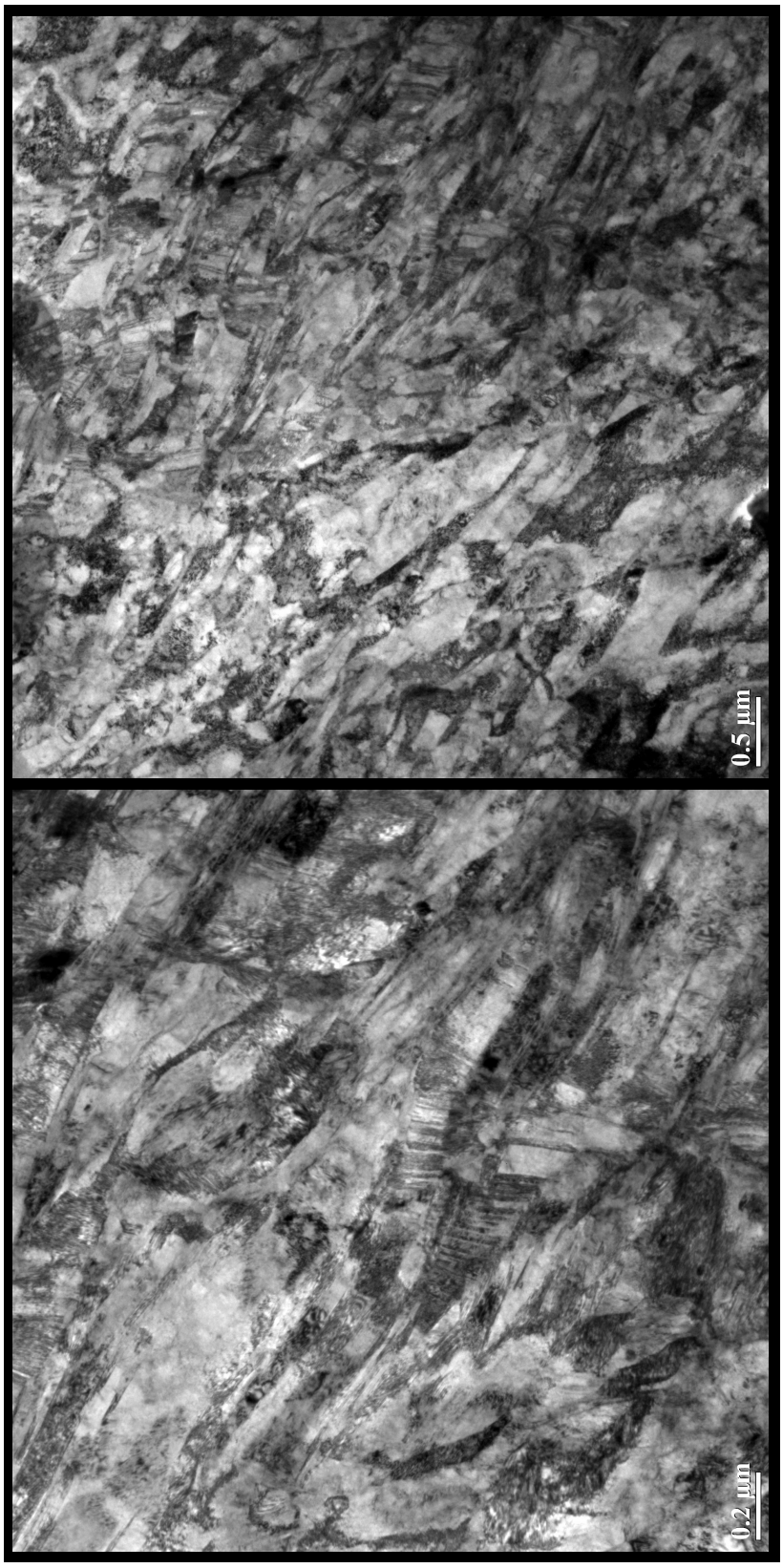

Figure 5.4 Continued.

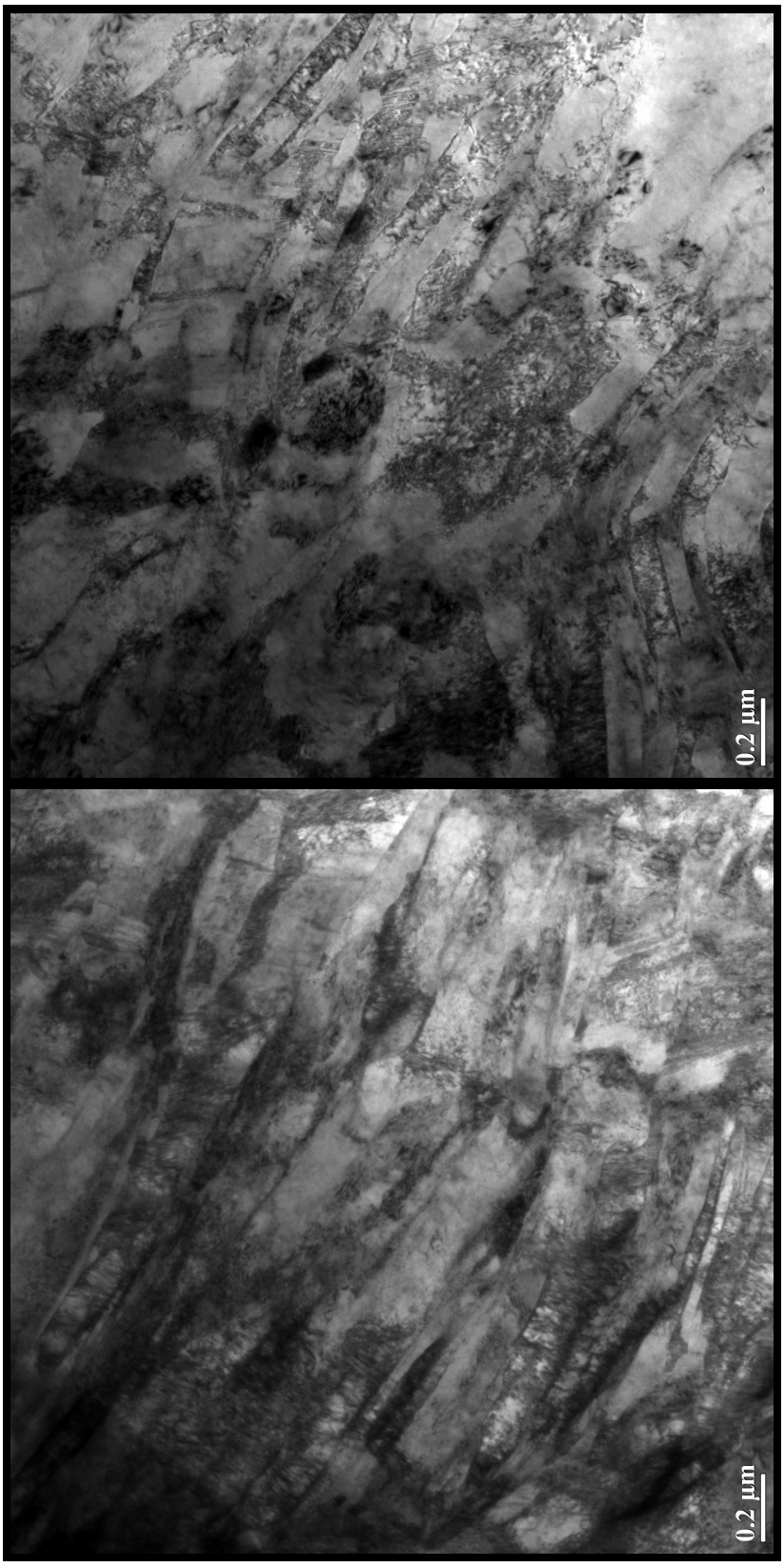

Figure 5.4 Continued.

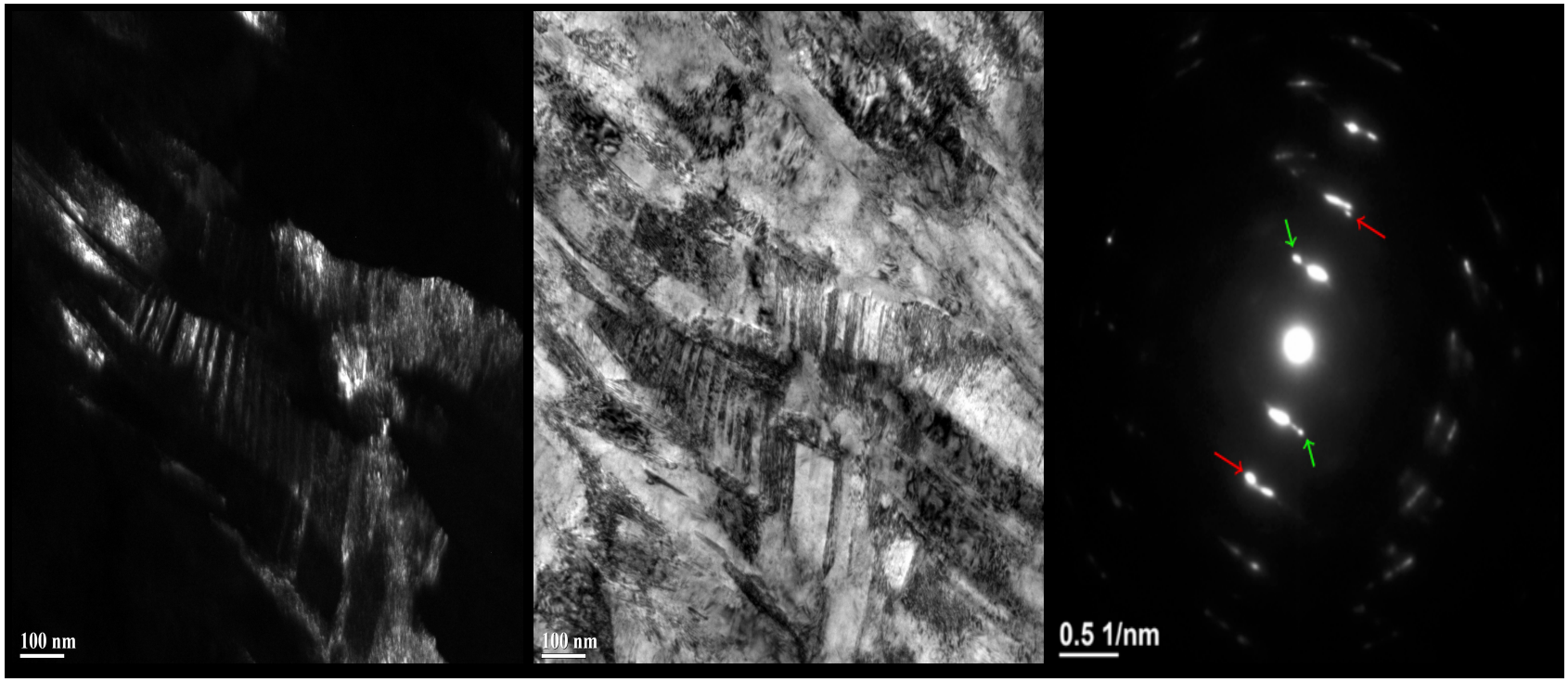

Figure 5.5 Bright-field, dark-field and the diffraction pattern of TEM images of 3C-900-700-500 °C processed material on the FP.

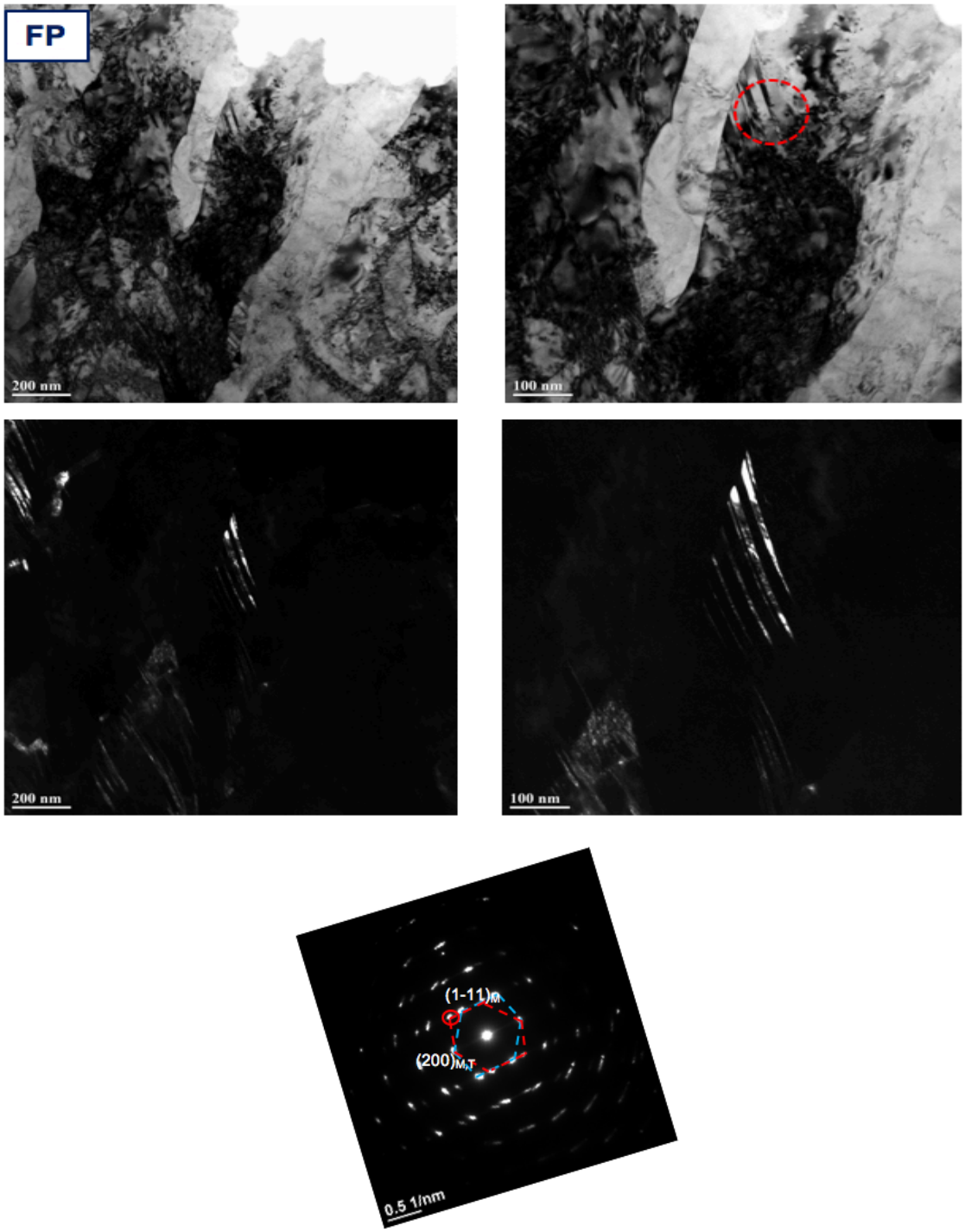

Figure 5.5 Continued.

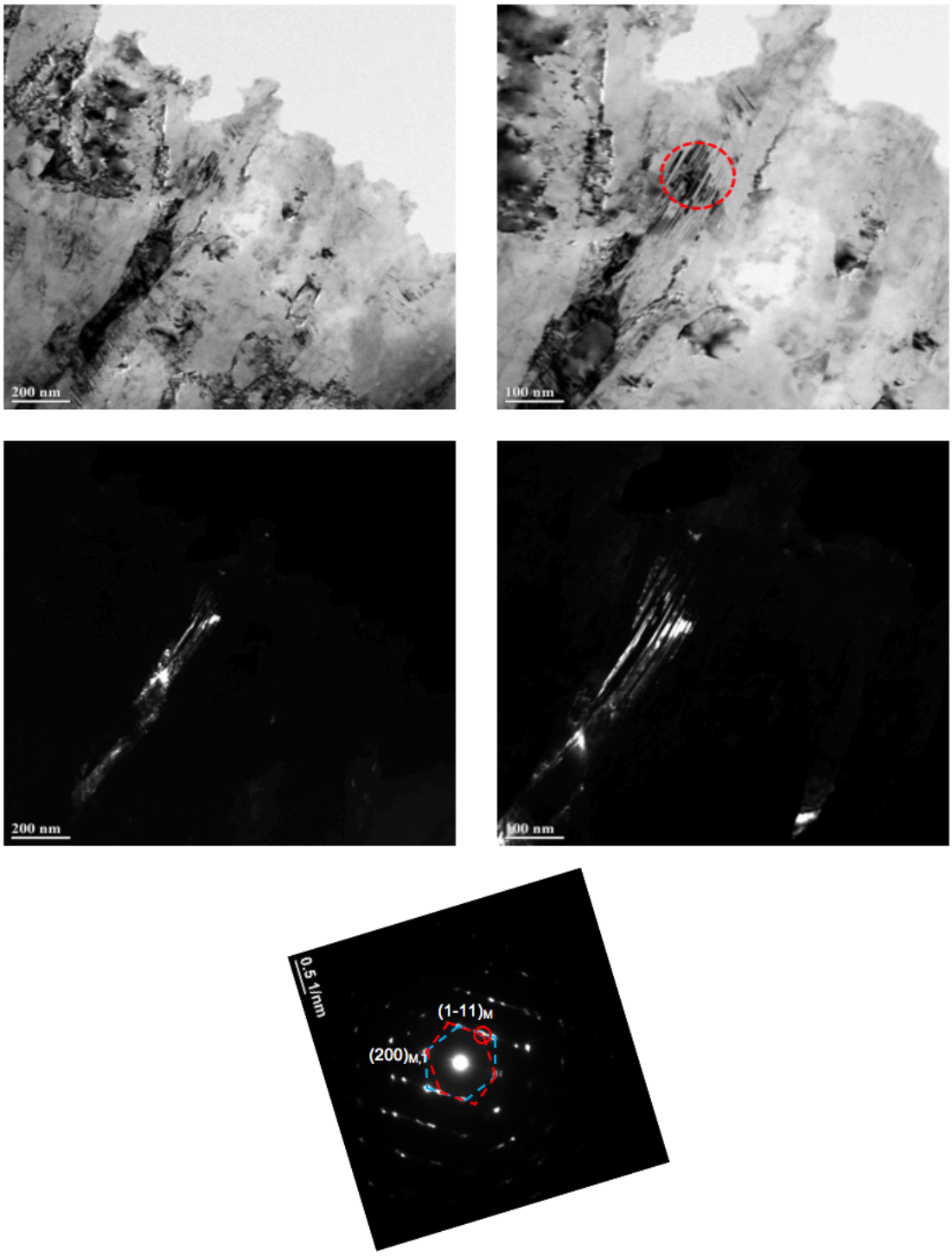

Figure 5.5 Continued.

5.3 Mechanical Behavior After ECAE

There was an incredible increase in the yielding stresses of the 3C-900-700-500 °C samples, which was more than 1 GPa for along FD. However, there was a drop in ductility of that as shown in Figure 5.6. Although the strongest as-processed material among others was fabricated, the ductility was below 1%. The yielding stress of the 3C-900-700-500 °C ECAE sample along the FD was almost 7 times greater than the as-received one. Some mechanical properties, such as ductility, depend on the orientation of the grains and the texture of the billets. As an additional study, the texture and grain orientation can be investigated in detail to understand the reason behind the low ductility. After ECAE, the as-cast porosity did not close down, so it was the solid evidence of why the low ductility material was processed.

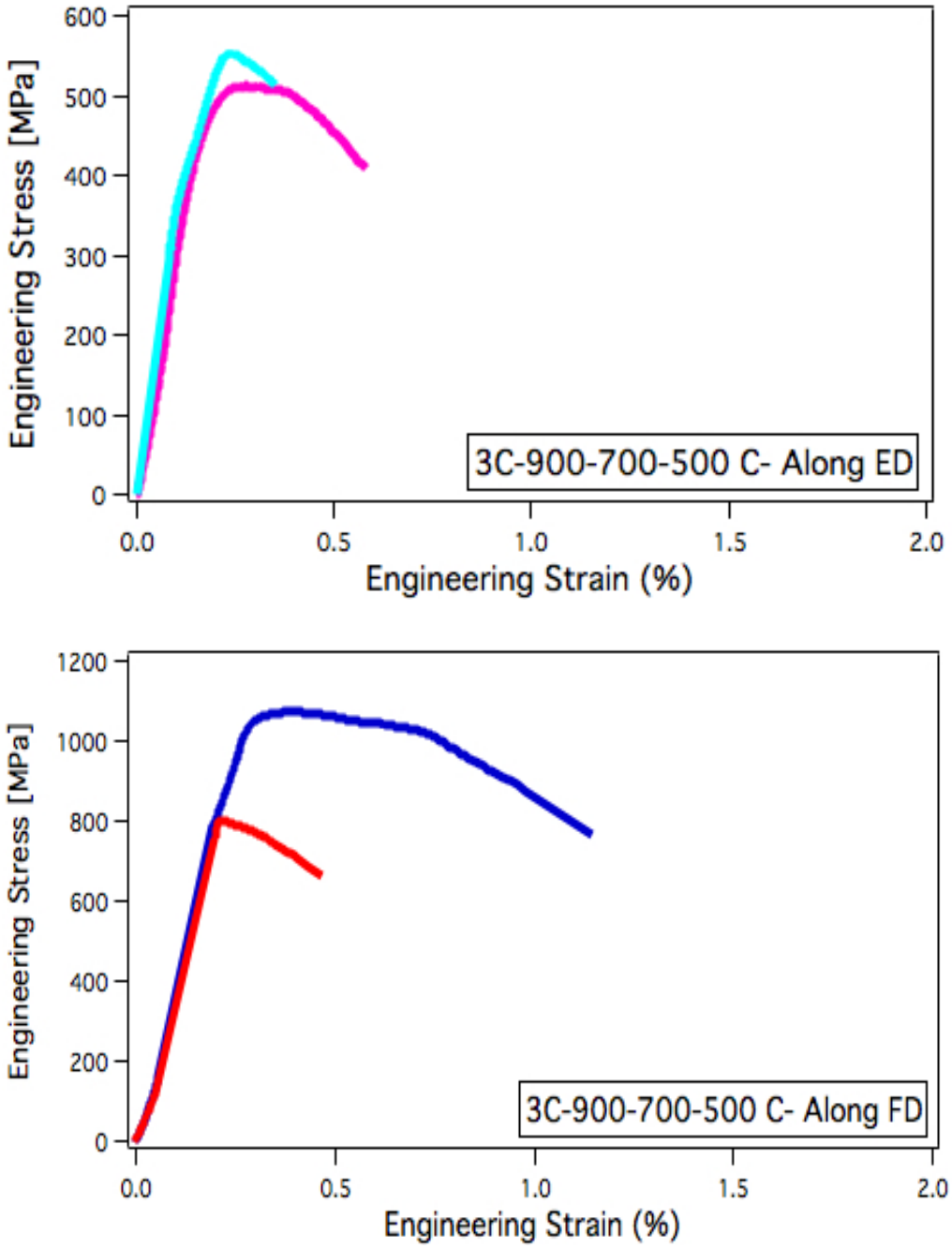

Figure 5.6 The tensile engineering stress-strain curves of the ECAE processed 3C-900-700-500 °C samples along the ED and the FD, respectively.

After all tests, the comparison of the results in terms of the SEM images and mechanical test would be necessary to figure out the differences between each as-ECEA-processed billet. Figure 5.7 shows how successfully grain refinement was achieved for each billet and for each plane. The images consisted of elongated and equiaxed grains, which means they were bimodal grains. The max grain refinement was achieved at 3C-900-700-500 °C on the EP due to one more C pass differently from other billets. For 3C-900-700-500 °C on the FP, there was some non-uniformity. Figure 5.8 indicated how microstructure evaluation was completed after the ECAE process. As can be seen, there were still pores after severe plastic deformation, which were not desirable results due to numerous reasons. Yet, the most important reason why porosities were unwanted microstructural defects was that they enormously affected the mechanical behavior of samples. In this research, as-cast porosity did not close down after the ECAE process and they were most likely to affect crack propagation during tensile tests as shown in Figure 5.9. The most brittle material was 3C-900-700-500 °C, whereas the most ductile one was 2C-900-1000 °C, among others.

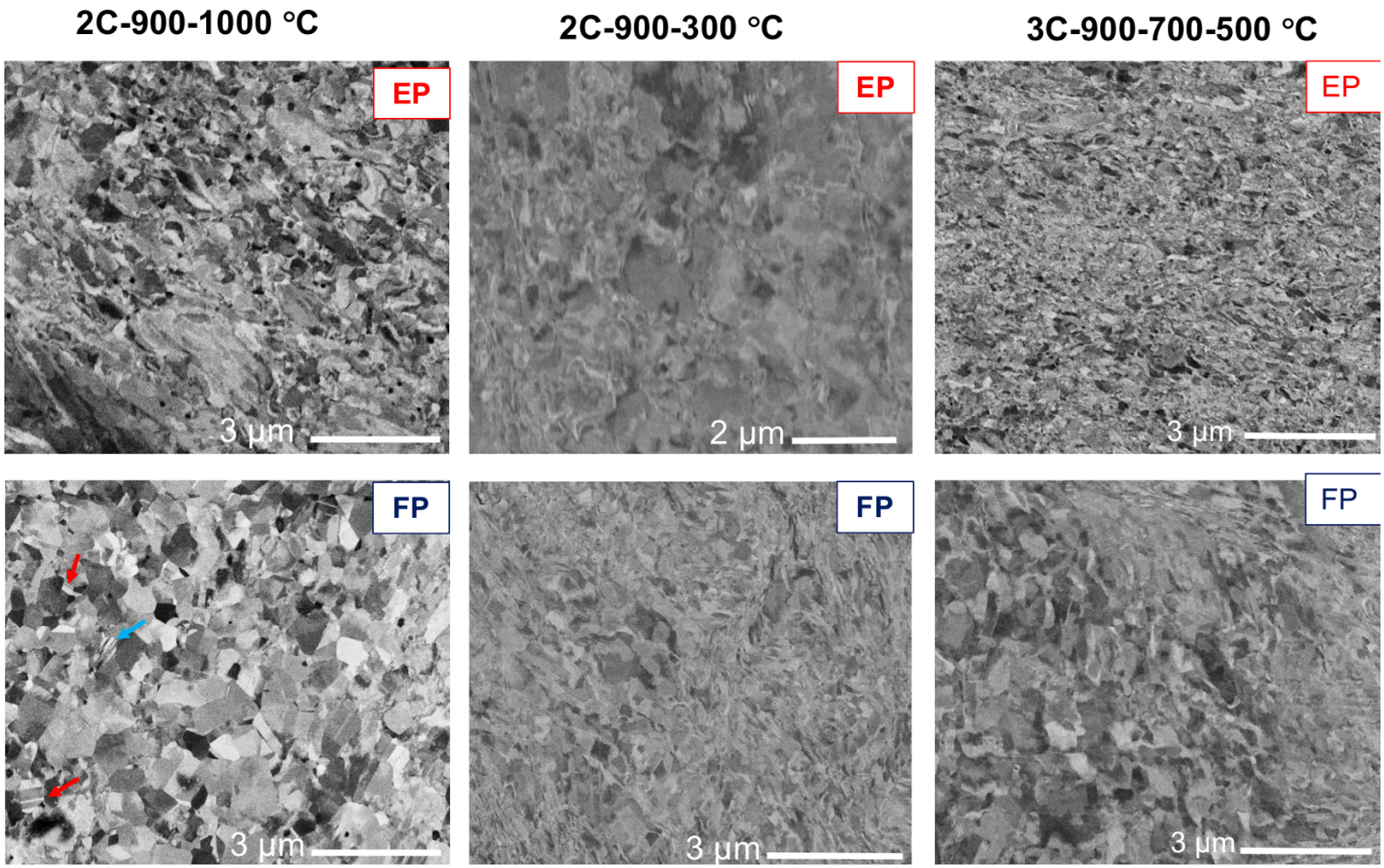

Figure 5.7 The comparison of SEM images of the as-processed billets.

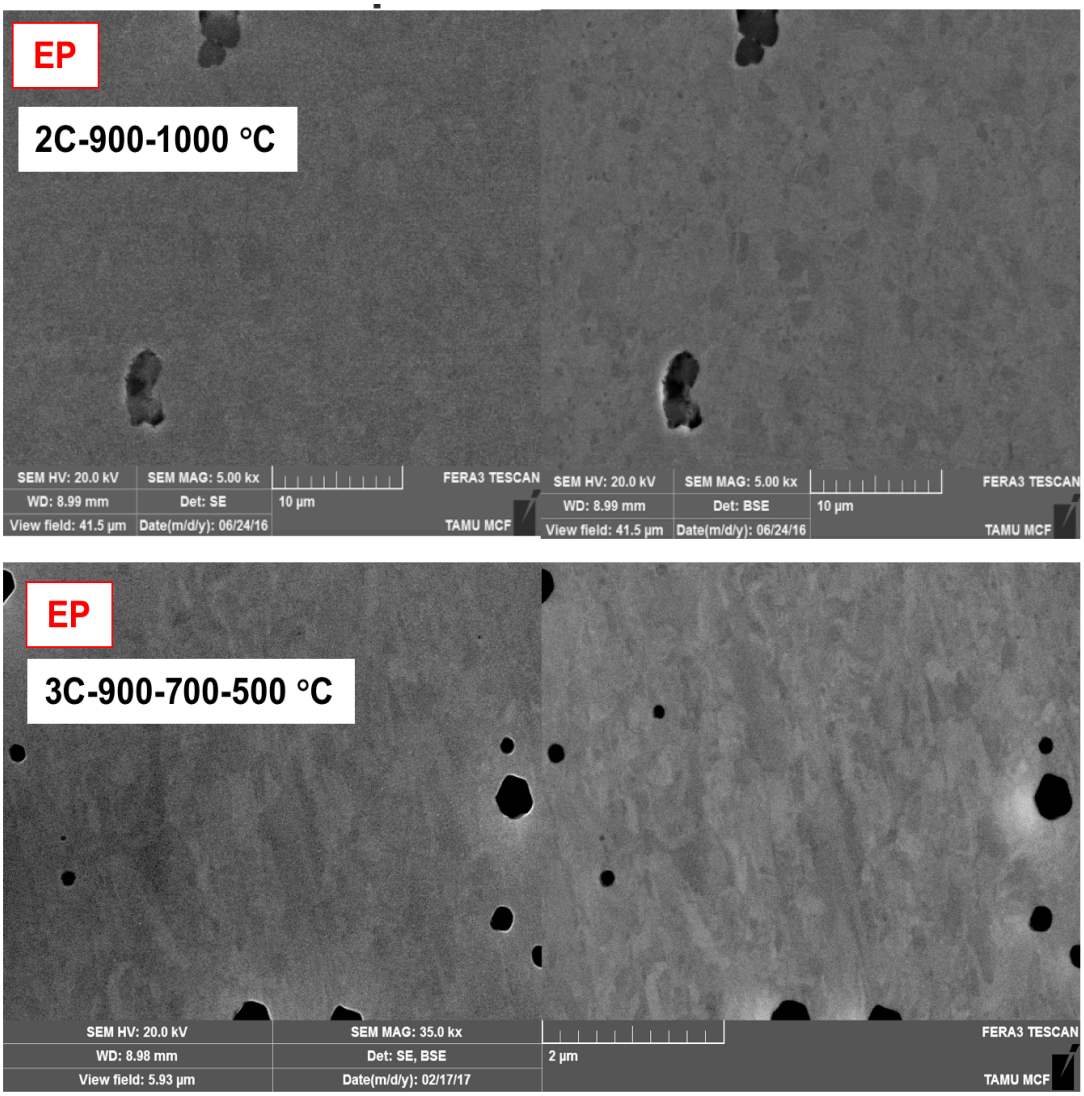

Figure 5.8 SEM images to show porosities after ECAE of 2C-900-1000 °C and 3C-900-700-500 °C on EP.

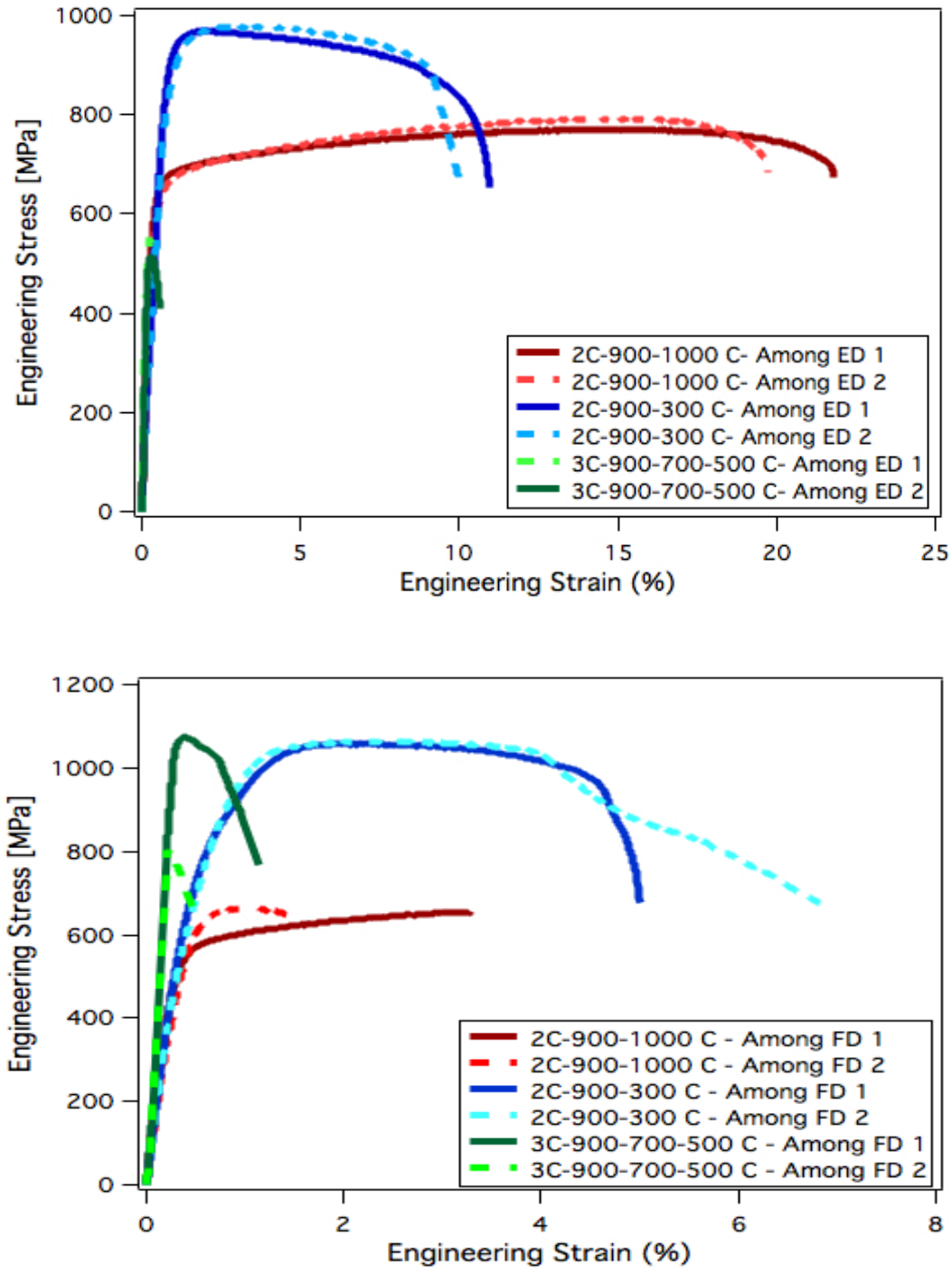

Figure 5.9 The comparison of all tension test result of billets along ED and FD.

CHAPTER VI

RESULTS AND DISCUSSIONS ON 2C-900-700 °C

Except for the last pass of 3C-900-700-500 °C billet, we followed the same procedure for this billet. We conducted totally two passes following Route A and Route C, respectively. Heat treatment was conducted for the as-received equiatomic CoCrFeMnNi HEA with the Argon backfill for two hours at 1200 °C to homogenize the sample before the ECAE process. Then, the billet was water quenched at room temperature. Afterwards, it was heated up to 900 °C for 30 minutes. Meanwhile, the ECAE die was preheated to 300 °C. The as-received CoCrFeMnNi billet was extruded at a rate of 0.5 inch/sec following Route A. After the first pass, the billet was water quenched to protect the microstructure that was successfully achieved during the ECAE process. For the second pass, the billet was reheated to 700 °C for 30 minutes and with the same extrusion rate, the second pass was not completed successfully following Route C. Figure 6.1 summarizes the all the conditions for 3C-900-700-500 °C. For this billet, due to lots of cracks we did not do any tests. As can be seen in Figure 6.2, the cracks proceed even at the center of the billet. It could be because of delamination, which is a kind of a failure of a material. High shear stress could cause delamination, which generally follows grain boundaries.

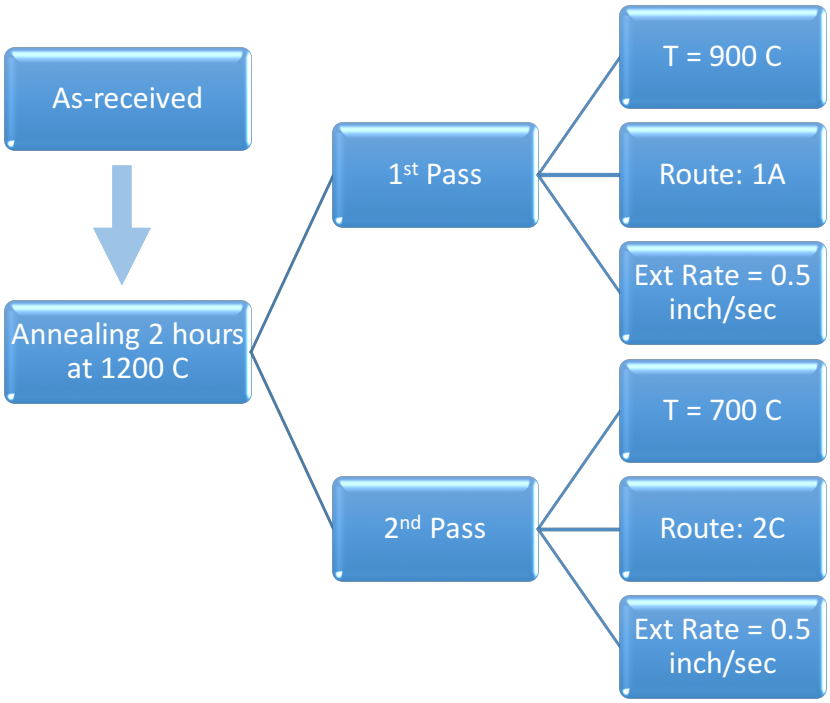

Figure 6.1 Flowchart of the ECAE processed 2C-900-700 °C material.

Figure 6.2 Extruded 2C-900-700 °C after two passes at 900 °C and 700 °C.

CHAPTER VII

CONCLUSIONS AND FUTURE DIRECTIONS

Near-equimolar quinary CoCrFeMnNi HEA was supplied from the company called Sophisticated Alloys in the form of a cylindrical rod with 1.25-inch diameter and 20-inch length. The alloy had a composition of 23.01% Co, 16.98% Cr, 19.79% Fe 18.85% Mn, 21.37% Ni and was fabricated by the vacuum induction melting technique under the Argon backfill. To fabricate ultra-fined grains from as-cast materials, Equal Channel Angular Extrusion (ECAE), which has been successful and feasible method, was used. The different microstructures, such as different grain size and different shaped-grains, were obtained after the ECAE process. The SEM studies were conducted to observe the microstructures of the extrusion plane and the flow plane of each billet. To interpret the deformation mechanisms, such as deformation twinning, another microstructural analysis was conducted by TEM after the ECAE process. In addition to microstructural analysis, mechanical tests were conducted in this research to interpret dependently the microstructure evaluation and mechanical behavior. Based on our observations, the following conclusions can be drawn for each billet.

<u>2C-900-1000 °C</u>

1. The mean grain size of 2C-900-1000 °C on the extrusion plane was 0.48 ± 0.16 μm, whereas on the flow plane this value was 0.67 ± 0.18 μm. Another observation about grains was their shapes. On the flow plane, the grains were more likely to be equiaxed, while on the extrusion plane, they were bimodal, which was a sign that

small part of the sample had some non-uniformity after severe plastic deformation.

2. On the flow plane, the deformation and the annealing twinning mechanisms were observed in the SEM studies.
3. Mechanical tests were performed for this samples along ED and FD several times. The tensile strains along ED was impressive for 2C-900-1000 °C which was greater than 20%. In addition to 20% strain, the yielding stress which was around 700 MPa along ED, was remarkable.
4. Along FD, there was a decrease in ductility and yielding stress for 2C-900-1000 °C because of the grains' orientations and the texture. Additional study about texture analysis is needed to understand the difference between tensile results of FD and ED.

2C-900-300 °C

1. On the extrusion plane, the average grain size of 2C-900-300 °C was 0.63 ± 0.1 μm, while on the flow plane this value was 0.43 ± 0.09 μm. Via the SEM studies, we concluded that on the extrusion plane, the shapes of the grains were equiaxed, while on the flow plane they were bimodal, which means grains were mixture of equiaxed and elongated grains with the different size.
2. On the flow plane, the TEM studies were conducted. The most important finding was that deformation twinning pairs were observed. This is the first time we observed twinning mechanisms at such a high temperature. The reason was that we achieved high rate deformation via the ECAE process so it caused deformation

twinning on the FP.

3. Mechanical tests were performed for this samples along ED and FD several times. The yielding stress was remarkable which was around 1 GPa along ED and more than 1 GPa along FD. As a result of the increased strength, a bit drop in ductility was as expected. Tensile strains along ED were greater than 10%, while that along FD were around 5%.
4. There was a decrease in ductility for 2C-900-300 °C along ED because of the grains' orientations and the texture. Further study about texture analysis is needed to understand the difference between tensile results of FD and ED.

3C-900-700-500 °C

1. The average grain size of 3C-900-700-500 °C on the EP was 0.29 ± 0.07 μm, while that on the FP was 0.57 ± 0.15 μm. After the SEM studies, we observed that on the extrusion plane the shapes of the grains were equiaxed, while on the flow plane, they were bimodal.
2. On the flow plane, the TEM studies were conducted. Again, for this sample, the most significant finding with the TEM studies was the observation of deformation twinning. As mentioned before, this is the first-time deformation twinning was detected at such high homologous temperatures because of high rate deformation caused by the ECAE process.
3. Again, mechanical tests were performed for this samples along ED and FD several times. The yielding stress was remarkable which was around 1 GPa along FD.

Surprisingly, there was a drop-in ductility and strength along ED compared with FD. The porosity was most likely to cause these drops.

4. Compared with other billet tensile test results, the strain rates were quite low. We thought that it could be because of one more C pass differently from other billets. Future research is needed to understand the reason behind low ductility behavior.

2C-900-700 °C

1. For this billet, due to lots of cracks we did not perform any tests.
2. As can be seen in Figure 6.2, the cracks proceed even at the center of the billet. It could be because of delamination which is a kind of failure. High shear stress could cause it, which generally follows grain boundaries.
3. To understand and investigate the reason behind the deep crack propagation, further study is necessary.

Although we gained a greater understanding of the effects of the ECAE deformation on equimolar CoCrFeMnNi HEA in this study, as a future study, we can perform some experiments to clarify the questions about this research. Based on what kind of clarification is needed, the following future directions can be drawn.

1. As-received material was used for the entire study, and porosity caused some issues. Therefore, instead of starting from as-cast material we should have started with wrought materials. We ordered new material and we applied hot extrusion in order to close down to porosity. Unluckily, we did not have time to process that

material. Therefore, we need to process this material to see the differences. With hot-extruded material, the results can be better in terms of ductility after the ECAE process.

2. The texture and the grains' distribution should be looked to investigate the results more deeply.
3. We need to populate more different processing by altering temperatures, routes, the number of passes and extrusion rates to observe the differences between each other.

REFERENCES

[1] Cantor, B., et al., *Microstructural development in equiatomic multicomponent alloys.* Materials Science and Engineering a-Structural Materials Properties Microstructure and Processing, 2004. **375**: p. 213-218.

[2] Yeh, J.W., *Recent progress in high-entropy alloys.* Annales De Chimie-Science Des Materiaux, 2006. **31**(6): p. 633-648.

[3] Yeh, J.W., *Alloy Design Strategies and Future Trends in High-Entropy Alloys.* Jom, 2013. **65**(12): p. 1759-1771.

[4] Yeh, J.W., et al., *Anomalous decrease in X-ray diffraction intensities of Cu-Ni-Al-Co-Cr-Fe-Si alloy systems with multi-principal elements.* Materials Chemistry and Physics, 2007. **103**(1): p. 41-46.

[5] Yeh, J.W., et al., *Formation of simple crystal structures in Cu-Co-Ni-Cr-Al-Fe-Ti-V alloys with multiprincipal metallic elements.* Metallurgical and Materials Transactions a-Physical Metallurgy and Materials Science, 2004. **35A**(8): p. 2533-2536.

[6] Yeh, J.W., et al., *Nanostructured high-entropy alloys with multiple principal elements: Novel alloy design concepts and outcomes.* Advanced Engineering Materials, 2004. **6**(5): p. 299-303.

[7] Murty, B.S., J.W. Yeh, and S. Ranganathan, *High-Entropy Alloys.* High-Entropy Alloys, 2014: p. 1-204.

[8] Guo, S. and C.T. Liu, *Phase stability in high entropy alloys: Formation of solid-solution phase or amorphous phase.* Progress in Natural Science-Materials International, 2011. **21**(6): p. 433-446.

[9] Cahn, R.W. and P. Haasen, *Physical metallurgy*. 3rd rev. and enl. ed. 2 volumes (xxxiv, 1957, 16 pages).

[10] Reed-Hill, R.E., *Physical metallurgy principles*. University series in basic engineering. x, 630 pages.

[11] Swalin, R.A., *Thermodynamics of solids. 2d ed. Richard A. Swalin*. Wiley series on the science and technology of materials. 1972: New York : J. Wiley, [1972]2d ed.

[12] Fisher, D.J., *High-Entropy Alloys - Microstructures and Properties*. Materials science foundations,. x , 154 pages.

[13] Gao, M.C., *High-entropy alloys : fundamentals and applications*. xiii, 516 pages.

[14] Shun, T.T., C.H. Hung, and C.F. Lee, *Formation of ordered/disordered nanoparticles in FCC high entropy alloys.* Journal of Alloys and Compounds, 2010. **493**(1-2): p. 105-109.

[15] Huang, P.K. and J.W. Yeh, *Inhibition of grain coarsening up to 1000 degrees C in (AlCrNbSiTiV)N superhard coatings.* Scripta Materialia, 2010. **62**(2): p. 105-108.

[16] Yang, X. and Y. Zhang, *Prediction of high-entropy stabilized solid-solution in multi-component alloys.* Materials Chemistry and Physics, 2012. **132**(2-3): p. 233-238.

[17] Senkov, O.N., et al., *Refractory high-entropy alloys.* Intermetallics, 2010. **18**(9): p. 1758-1765.

[18] Kao, Y.F., et al., *Electrical, magnetic, and Hall properties of AlxCoCrFeNi high-entropy alloys.* Journal of Alloys and Compounds, 2011. **509**(5): p. 1607-1614.

[19] Lu, C.L., et al., *Thermal expansion and enhanced heat transfer in high-entropy alloys.* Journal of Applied Crystallography, 2013. **46**: p. 736-739.

[20] Tsai, K.Y., M.H. Tsai, and J.W. Yeh, *Sluggish diffusion in Co-Cr-Fe-Mn-Ni high-entropy alloys.* Acta Materialia, 2013. **61**(13): p. 4887-4897.

[21] Hsu, C.Y., et al., *On the superior hot hardness and softening resistance of AlCoCrxFeMo0.5Ni high-entropy alloys.* Materials Science and Engineering a-Structural Materials Properties Microstructure and Processing, 2011. **528**(10-11): p. 3581-3588.

[22] Juan, C.C., et al., *On microstructure and mechanical performance of AlCoCrFeMo0.5Nix high-entropy alloys.* Intermetallics, 2013. **32**: p. 401-407.

[23] Liu, W.H., et al., *Grain growth and the Hall-Petch relationship in a high-entropy FeCrNiCoMn alloy.* Scripta Materialia, 2013. **68**(7): p. 526-529.

[24] Otto, F., et al., *Decomposition of the single-phase high-entropy alloy CrMnFeCoNi after prolonged anneals at intermediate temperatures.* Acta Materialia, 2016. **112**: p. 40-52.

[25] Otto, F., et al., *The influences of temperature and microstructure on the tensile properties of a CoCrFeMnNi high-entropy alloy.* Acta Materialia, 2013. **61**(15): p. 5743-5755.

[26] Otto, F., N.L. Hanold, and E.P. George, *Microstructural evolution after thermomechanical processing in an equiatomic, single-phase CoCrFeMnNi high-*

entropy alloy with special focus on twin boundaries. Intermetallics, 2014. **54**: p. 39-48.

[27] Otto, F., et al., *Relative effects of enthalpy and entropy on the phase stability of equiatomic high-entropy alloys.* Acta Materialia, 2013. **61**(7): p. 2628-2638.

[28] Senkov, O.N., et al., *Mechanical properties of Nb25Mo25Ta25W25 and V20Nb20Mo20Ta20W20 refractory high entropy alloys.* Intermetallics, 2011. **19**(5): p. 698-706.

[29] Tong, C.J., et al., *Microstructure characterization of AlxCoCrCuFeNi high-entropy alloy system with multiprincipal elements.* Metallurgical and Materials Transactions a-Physical Metallurgy and Materials Science, 2005. **36A**(4): p. 881-893.

[30] Tsai, C.W., et al., *Deformation and annealing behaviors of high-entropy alloy Al0.5CoCrCuFeNi.* Journal of Alloys and Compounds, 2009. **486**(1-2): p. 427-435.

[31] Ranganathan, S., *Alloyed pleasures: Multimetallic cocktails.* Current Science, 2003. **85**(10): p. 1404-1406.

[32] Gali, A. and E.P. George, *Tensile properties of high- and medium-entropy alloys.* Intermetallics, 2013. **39**: p. 74-78.

[33] Lowe, T.C. and R.Z. Valiev, *Investigations and applications of severe plastic deformation*. NATO ASI series Partnership sub-series 3, High technology. xix, 394 pages.

[34] Valiev, R.Z., R.K. Islamgaliev, and I.V. Alexandrov, *Bulk nanostructured materials from severe plastic deformation.* Progress in Materials Science, 2000. **45**(2): p. 103-189.

[35] Gleiter, H., *Nanocrystalline materials.* Progress in Materials Science, 1989. **33**(4): p. 223-315.

[36] Segal, V.M., *Materials processing by simple shear.* Materials Science and Engineering a-Structural Materials Properties Microstructure and Processing, 1995. **197**(2): p. 157-164.

[37] Segal, V.M., et al., *Plastic working of metals by simple sheaR.* Russian Metallurgy, 1981(1): p. 99-105.

[38] Cornwell, L.R., et al., *The equal channel angular extrusion process for materials processing.* Materials Characterization, 1996. **37**(5): p. 295-300.

[39] Ferrasse, S., et al., *Microstructure and properties of copper and aluminum alloy 3003 heavily worked by equal channel angular extrusion.* Metallurgical and Materials Transactions a-Physical Metallurgy and Materials Science, 1997. **28**(4): p. 1047-1057.

[40] Laplanche, G., et al., *Microstructural evolution of a CoCrFeMnNi high-entropy alloy after swaging and annealing.* Journal of Alloys and Compounds, 2015. **647**: p. 548-557.

[41] Yoshida, S., et al., *Friction stress and Hall-Petch relationship in CoCrNi equi-atomic medium entropy alloy processed by severe plastic deformation and subsequent annealing.* Scripta Materialia, 2017. **134**: p. 33-36.